5-1-2012

Applications of Voronoi partitions in particle therapy

Daniel Riofrio

Daniel Andrés Riofrío Almeida

Candidate

Computer Science

Department

This thesis is approved, and it is acceptable in quality and form for publication:

Approved by the Thesis Committee:

Shuang Luan , Chairperson

Michael Holzscheiter

Philip Heintz

Applications of Voronoi Partitions in Particle Therapy

by

Daniel Andrés Riofrío Almeida

Ingeniero en Sistemas Informáticos y de Computación,
Escuela Politécnica Nacional,
Quito-Ecuador, 2005

THESIS

Submitted in Partial Fulfillment of the
Requirements for the Degree of

Master of Science
in
Computer Science

The University of New Mexico

Albuquerque, New Mexico

May, 2012

Dedication

To Mom, Dad, Carlos, María Cris, and Daniela.
Thank you so much for all your support.
Im memoriam of my old friend Pedro Pablo Maldonado Omat
Hasta siempre mi buen amigo.

Acknowledgments

I would like to thank all the people that contributed to the development of this thesis, specially, to my advisor, Prof. Shuang Luan, for his support, trust, and all his time and dedication helping me finish this thesis; to Oliver Jäkel, from the University of Heidelberg Department of Radiation Oncology and Radiotherapy, for suggesting the beam energy modulation minimization problem that started this research; to Prof. Michael Holzscheiter from the Max Planck Institute for Nuclear Physics (MPI-K) for suggesting the LET painting problem. In addition, I would like to thank Roy Keyes for his help in generating Fluka kernels used widely in the simulations as well as Stefan Sellner and Gonzalo Cabal from the DKFZ (the German Cancer Reserach Center) and, Niels Bassler Department of Clinical Experimental Oncology at Aarhus University Hospital, Denmark for all their thoughtful and useful comments.

This thesis was partially supported by NSF grants CBET-0755054 and CBET-0853157 as well as the Ecuadorian "Fulbright & Senescyt" scholarship. Part of this research was presented in the 2011 AAPM/COMP Joint Meeting in Vancouver, Canada which was made possible by travel and research grants from the UNM Graduate and Professional Student Association (GPSA-SRAC) and UNM Office of Graduate Studies (OGS-RPT).

Last but not least, I would like to thank my family and friends, and specially to my girlfriend Daniela, for all her love.

Applications of Voronoi Partitions in Particle Therapy

by

Daniel Andrés Riofrío Almeida

Ingeniero en Sistemas Informáticos y de Computación,

Escuela Politécnica Nacional,
Quito-Ecuador, 2005

M.S., Computer Science, University of New Mexico, 2012

Abstract

Treating cancer using charged particles heavier than electrons is becoming more and more popular in modern cancer management due to its increased dose to the targeted tumors and improved sparing of surrounding normal tissues and critical structures. Many challenging and interesting mathematical optimization problems arise in the planning of charged particle radiation therapy. In this thesis, we study three important optimization problems in particle therapy, which includes *dose optimization*, *energy modulation change reduction*, and *LET (linear energy transfer) painting*.

Generally speaking the goal of treatment planning is to use computer based algorithms and software to find a therapeutic plan that maximizes the "dose" delivered to the target tumor while at the meantime minimizing that to the surrounding normal tissues and critical structures. The word "dose" here can refer to physical dose, i.e., energy imparted by the incoming ionizing radiation to the patient, radiobiological

dose such as percentage of cells killed, or a combination of both. As an example, the *LET painting problem* that we studied can be viewed as a combination of physical dose and radiobiological dose, because the LET distribution of a treatment plan can be viewed as a "surrogate" for beam quality and increasing the LET can lead to increased cell killing efficiency under certain circumstances. Various machine properties are also considered in these optimizations. In most particle facilities, changing the beam energies requires an undesirable delay; therefore, in the *energy modulation change reduction* we aim to reduce the number of energy changes without compromising the final physical dose distribution.

The contributions of this thesis include the following. (1) We have developed a parameterizable prototype treatment planning system for physical dose optimizations which implements kernel based dose calculations for non-uniform mediums, and dose optimization using non-negative least squares. (2) We found that Voronoi partitions can provide effective heuristic solutions to the *energy modulation change reduction* and *LET painting* problems. In addition, this thesis also identified an array of important and challenging computational problems that are not only of importance to the clinicians but also of considerable interests to computer scientists.

Contents

List of Figures

List of Figures

List of Tables

Glossary

Anti-proton	is a charged particle with the same mass and opposite exact charge as a proton. It is the anti particle of proton and is represented by the symbol $\bar{p}$ [8].
Chemotherapy	is the (invasive) use of drugs (chemicals) to target cells that reproduce rapidly such as cancer cells.
Dose	is defined as the amount of energy deposited per unit mass (for more details, see section 2.2.2).
DVH	Dose volume histogram is a tool used to understand the quality of a treatment plan in terms of its dose distributions. It provides the amount of volume per biological structure that received at least a certain percentage of the maximum dose.
FLUKA	is a Monte Carlo tool for simulate particle interactions with matter. It is the result of a combined effort of the Italian National Institute for Nuclear Physics (INFI) and the European Organization for Nuclear Research (CERN).
GEANT4	is a Monte Carlo open source code toolkit for simulating particle interactions with matter. It is the result of a combined effort of the European Organization for Nuclear Research (CERN), European

	Space Agency (ESA), Istituto Nazionale di Fisica Nucleare (INFI), Jefferson Lab, KEK, among others [9, 10].
Ionization	is the effect of physically adding or removing orbital electrons from an atom converting it into an ion.
IMRT	Intensity-modulated radiation therapy is an irradiation technique that uses non-uniform beam intensities for delivering highly conformal dose to a localized tumor while sparing healthy tissues.
LET	Linear Energy Transfer is a measurement of dose quality. It is defined as the ratio between a differential energy lost by a charged particle and a differential length of its track (for more details, see section 2.2.4).
Proton	is a fundamental particle that constitutes matter. It was named by Niels Bohr in 1914 when he referred to the nucleus of the lightest atom (hydrogen) [8]. This atom is characterized by possessing one electron (e^-) orbiting a nucleus of one proton (p^+).
LVH	LET volume histogram is a tool used to understand the quality of a treatment plan in terms of LET. It provides the amount of volume per biological structure that received at least a certain LET relative to the highest calculated LET.
RBE	Radiobiological effectiveness is the ratio of two different dose types that produce the same cell damage (for more details, see section 2.2.5).
Stopping Power	is the expected kinetic energy loss by a charged particle along its track while interacting with matter (for more details, see section 2.2.3).

Voronoi Partition or tessellation is a special partition of a given space determined by distances to a specified collection of objects, where to each object one associates a corresponding Voronoi cell containing the portion of the given space whose distance to the given object is no greater than its distance to the other objects. It is named after the Russian mathematician Georgy Voronoy (for more details, see section 3).

Chapter 1

Introduction

Cancer is a wide spread disease that expresses itself through the errant growth of abnormal cells. If the uncontrolled growth of these cells is not stopped, it can cause death [11, 12]. As the worldwide cancer's fatal trend increases, in 2010 alone, there were 571,950 deaths due to cancer in America, which was more than 1,500 people per day [12]. This along with the estimated cost of $263.8 billion USD for cancer management [13, 12] has led to an increased demand from the general public to develop more effective tools and technologies for curing cancer.

The focus of this thesis is radiation therapy and radiosurgery, which is one of our most effective means to treat local-regional tumors. Today, radiotherapy in combination with surgery accounts for more than 50% of the treatments. With the rapid advancement of medical imaging, more and more tumors are being diagnosed in early stages when they are still local or regional. Hence, one can only expect the percentage of patients going through radiation therapy to increase.

Radiation therapy is a modality of cancer treatment with ionizing radiations. The ionizing radiation (e.g., high energy X-rays) damages the DNA and causes cell death within the region being irradiated. Hence, the goal of radiation therapy is to

deliver a radiation dose high enough to kill all the targeted tumor cells while simultaneously minimizing the damage to surrounding normal structures. The quality of a radiotherapy plan is usually judged by its *dose conformity* and *treatment time*. The dose conformity describes how well the high radiation dose region conforms to the targeted tumor and spares the surrounding normal tissues, while the treatment time describes how long the treatment takes and how efficient the treatment machines are used. Any improvement on the dose conformity in radiation therapy will likely improve tumor control and reduce the likelihood of complications, and any improvement in treatment time will likely lower the treatment cost and improve patient throughput and comfort.

Many types of ionizing radiations have been experimented along the history of radiotherapy. These include high energy photons (e.g., $\gamma-$rays and high energy x-rays), electrons, and charged particles heavier than electrons such as protons, pions, alpha particles, carbon ions, and even antiprotons. Generally speaking, the advantage of charged particles heavier than electrons (also referred to as hardons) over high energy photons can be attributed to their distinct energy deposition patterns. As shown in Figure 1.1, as photons pass through the body, the energy deposited is exponentially decreasing, resulting in a high entry dose. As a result, it is often the case that the amount of dose deliverable to the tumor is higher than that in the tumor, which may lead to acute side effects and can potentially cause secondary cancer years after the initial treatment. In contrast, heavier charged particles such as carbon ions show little interaction when they first enter the medium and deposit the dominant portion of their energy only close to the end of their range. This leads to an inverse dose profile, exhibiting a well-defined peak of energy deposition, called the Bragg Peak. (The depth of the Bragg Peak depends on the energy of the initial particles.) This allows for a significant reduction of dose delivered outside the primary target volume and leads to substantial sparing of normal tissue and nearby organs at risk.

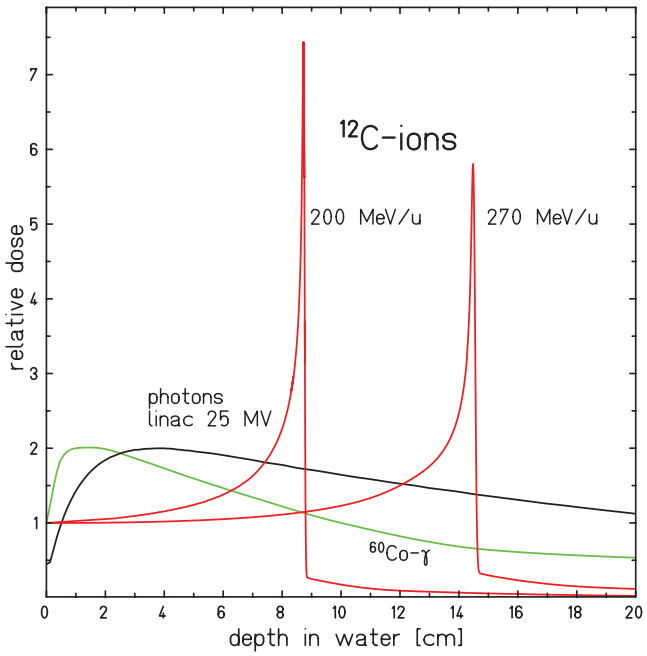

Figure 1.1: Depth-dose diagram: Comparison between photon and carbon beams [1].

In this thesis we focused on charged particle therapies. Specifically, we studied three mathematical optimization problems that arise in charged particle therapy. These problems include *dose optimization*, *energy modulation change reduction*, and *LET painting*.

Dose Optimization: The goal of dose optimization is to create a physical dose distribution whose high dose regions conforms to the targeted tumor while in the meantime minimizing the dose deposition outside the target.

Energy Modulation Change Minimization: The depth of the Bragg Peak (see Figure 1.1) is controlled by the energy of the beam's primary particles. Thus by varying the energy, we can create a dose distribution that is conformal to the target volume. However, changing beam energies in particle therapy requires an undesirable delay; therefore, a high quality treatment plan with minimum number of energy changes is desired, which is the goal of energy modulation change minimization.

LET painting: Most radiation therapies delivered in today's clinic are planned based on physical dose distributions alone. However, when delivering a photon beam and a heavy charged particle (e.g., carbon ion) beam to the body, even with the same amount of physical energy deposited, the induced biological damage is typically not the same. This is because photons usually give rise to secondary electrons that are sparsely distributed along the photon path, while heavier particles, such as carbon ions result in a dense distribution of ionization events. While photons produce on a scale of typical cell dimensions an evenly spread low dose distribution, heavy charged particles produce a very high dose on a microscopic scale, comparable to the size of the DNA, which can inflict significant local damage to the cell. A good physical concept to quantify the ionization density of different types of radiation is the concept of *linear energy transfer (LET)* [2, 14]. Figure 1.2 shows the LET distribution of a 150 $[MeV]$ proton beam. Sparsely ionizing particles such as photons ($X-$ and $\gamma-$rays) have a lower LET as compared to densely ionizing radiation such as heavy ions. LET and physical dose are complimentary to each other and combining them in planning could be a significant improvement [14, 15, 16, 17, 18]. Generally speaking, the goal of *LET painting* is to localize the high LET region inside the tumor while producing the required conformal physical dose distribution.

In this research, we explore using Voronoi diagrams to solve these optimization problems. A Voronoi diagram segments a given space under a provided metric. Our intuition is the tumor cells should be treated using their "nearest" beams. For LET painting, since the high-LET region of a charged particle beam is located at the distal edge of its Bragg peak, if a beam stops at the center of the target, its high LET region is also likely inside the target. Thus making lower energy beams more preferable than high energy beams. On the other hand, for dose and energy modulation change the key observation lies in the fact that the depth of the Bragg Peak is a function of energy, then selecting the beam "closest" to a voxel implies the selection of beams that traverse less tissue which may reduce the number of energy changes.

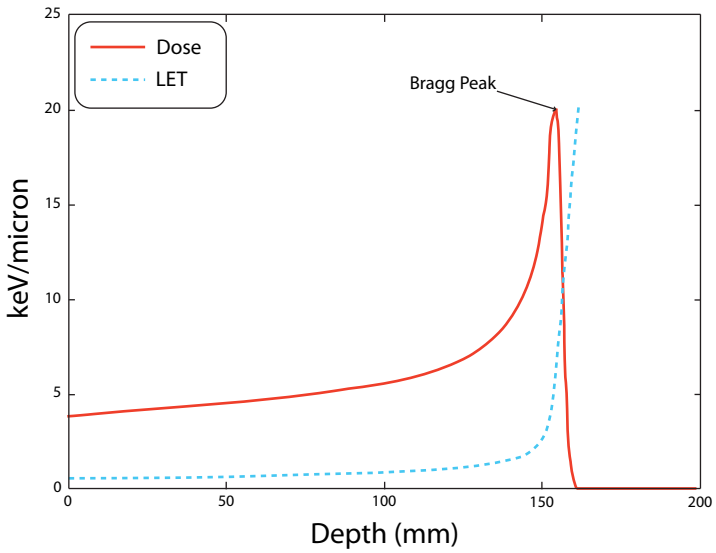

Figure 1.2: LET and depth-dose diagram for a 150 $[MeV]$ proton beam.

The following is a summary of the contributions of this thesis. (1) We have developed a parameterizable prototype treatment planning system for physical dose optimizations which implements kernel based dose calculations for non-uniform mediums using water-equivalent path length (for more information about this topic see section 2.2.7), and dose optimization using non-negative least squares. (2) We found that Voronoi partitions can provide effective heuristic solutions to the energy modulation change reduction and LET painting problems. In addition, this thesis also identified an array of important and challenging computational problems that are not only of importance to the clinicians but also of considerable interests to computer scientists. These problems will lay the foundation of my future Ph.D. study.

The rest of the thesis is organized as follows. Chapter 2 presents a brief overview on Radiation Therapy with a special focus on particle therapy and provides basic physics concepts such as fluence, dose, stopping power, linear energy transfer, relative biological effectiveness, and water-equivalent path length. Chapter 3 introduces

Voronoi partitions and provides a brief walk-through its computational complexity and some classical algorithms. Chapter 4 describes the concept of a treatment planning system (TPS) and in particular our treatment planning system prototype. Chapter 5 presents our solution to the beam energy modulation reduction and the simultaneous dose and LET painting problems. Finally, Chapter 6 concludes the thesis and discusses some exciting computational problems for my future Ph.D. dissertation.

Chapter 2

Radiation Therapy

2.1 Overview

Radiological physics is the science that studies ionizing radiation and its interaction with matter. The field began in the 1890s immediately following the discovery of X-rays by Wilhelm Röntgen [19], radioactivity by Henri Becquerel [20], and radium by the Curies [21]. The most important types of ionizing radiations for therapeutic usage are γ-rays, X-rays, fast electrons (positrons, β-rays, δ-rays), ions (protons, deuterons, tritons, alpha particles, pions, etc.), and neutrons [22, 2, 3, 23].

Since the focus of this thesis is particle radiation therapy, here we provide some background knowledge. The chapter is organized as follows. Section 2.2 introduces some basic physical concepts. Section 2.3 presents a concise overview of treatment planning of radiation therapy and defines the optimization model. Finally, Section 2.4 describes the model of particle therapy in this thesis.

2.2 General Concepts

2.2.1 Fluence

Given a beam of particles, the **fluence** Φ is defined to be number of particles passing through a unit area during a time interval of interest. Mathematically, fluence is defined using equation 2.1, where N is the total number of particles passing through an area A. As a result, the unit for fluence is $\left[\frac{1}{m^2}\right]$

$$\Phi = \frac{N}{A} \tag{2.1}$$

2.2.2 Dose

One of the most important concepts in radiological physics is **absorbed dose** (or simply **dose**). Generally speaking, the absorbed dose D is the amount of energy deposited in medium per unit mass. Equation 2.2 shows the mathematical definition of dose, where $\mathrm{d}E$ is the differential of energy deposited in a mass differential $\mathrm{d}m$. The SI unit for absorbed is $\left[\frac{J}{kg}\right]$ or gray $[Gy]$[3].

$$D = \frac{\mathrm{d}E}{\mathrm{d}m} \tag{2.2}$$

2.2.3 Stopping power

The stopping power S of a charged particle is defined to be its expected kinetic energy loss, $\mathrm{d}E$, along the particle track, $\mathrm{d}x$ (see equation 2.3). The stopping power

S depends on the type of the particle Y, its energy E, and the atomic number Z of the medium. The unit commonly used for expressing stopping power is $\left[\frac{keV}{\mu m}\right]$ [22].

$$S = \left(\frac{\mathrm{d}E}{\mathrm{d}x}\right)_{Y,E,Z} \tag{2.3}$$

2.2.4 Linear Energy Transfer (LET)

Interested readers may question the relation between stopping power and dose. It turns out that not all the energy lost by the charged particles is deposited locally and contributes to dose. Some form of this energy loss is converted to secondary particles (e.g., high energy electrons or photons) that travel much further away. Thus to calculate dose, one needs to remove the portion of the energy loss in $\mathrm{d}E$ in equation 2.3 that is not deposited locally. This gives rise to the concept of **linear energy transfer**, which is also referred to as the **restricted stopping power**. Precisely, the linear energy transfer (LET) is a measure of local energy deposition along the particle track and is defined in equation 2.4, where Δ reflects the restriction of the energy loss that is deposited locally [22, 17].

$$L_\Delta = \left(\frac{\mathrm{d}E}{\mathrm{d}x}\right)_\Delta. \tag{2.4}$$

Equation 2.5 puts the concepts of dose, LET and fluence into perspective, where the local dose is simply the product of fluence and the LET if the particles are of the same type and energy.

$$D = \Phi L_\Delta. \tag{2.5}$$

In the situation where the particle fluence consists of a spectrum of particles of different energies, i.e., $\Phi(E)$, one will need to integrate over the energy spectrum as in equation 2.6 in order to calculate the dose.

$$D = \int \Phi(E) L_{\Delta}(E) dE. \tag{2.6}$$

When it comes to calculating the LET of a beam of particles, one can either invoke the **track averaged LET** or **dose averaged LET**.

Track averaged LET L_t of a beams of particles simply average the LET over the fluence (see equation 2.7)[15, 16].

$$L_t = \frac{\int \Phi(E) L_{\Delta}(E) dE}{\int \Phi(E) dE} \tag{2.7}$$

The dose averaged LET L_d is the cumulative LET weighted by the local dose contributions of the particle (see equation 2.8). Note that the term $\Phi(E)L_{\Delta}(E)$ is the local dose contribution from the particles with energy E, while $\int \Phi(E)L_{\Delta}(E)dE$ is the total local dose as in equation 2.6 [15, 16].

$$L_d = \frac{\int (\Phi(E) L_{\Delta}(E)) L_{\Delta}(E) dE}{\int \Phi(E) L_{\Delta}(E) dE} \tag{2.8}$$

2.2.5 Relative biological effectiveness (RBE)

Relative biological effectiveness is defined as the ratio of a control radiation dose, D_0, and some test radiation, D_r such that the cell damaged for both radiations is

the same (see equation 2.9) [2].

$$RBE_r = \frac{D_0}{D_r}. \tag{2.9}$$

Generally, the control radiation corresponds to a X-ray beam. According to the NBS (The National Bureau of Standards) 1954 standard (now NIST, National Institute of Standards and Technology), this control radiation comes from a 250 $[keV]$ X-ray beam [2]. Nonetheless, in practice, the reference is often $\gamma-$rays from cobalt-60 isotope (^{60}Co).

2.2.6 RBE as a function of LET

Radiobiological experiments have shown a positive correlation between the RBE and the LET [17]. Intuitively, this can be explained by the fact that ionizing radiation causes cell DNA damage by either directly ionizing the DNA molecules or indirectly through ionized water molecules. These damages may induce DNA strand breaks and thus disrupting the reproductive cycle of cells and eventually lead to cell death [24]. In order to induce this damage, energy needs to be transferred from the incident particles into the medium. Since the damage is a probabilistic event, the denser the energy exchange, the more likely the damage is to occur. Figure 2.1 shows the positive correlation between increased RBE as a function of LET [2, 25].

It is also worth noting that when the LET is beyond a certain threshold e.g., 100 $\left[\frac{keV}{\mu m}\right]$) the RBE decreases. This effect is known as the "overkill effect" [26, 27]. One explanation of the overkill effect is that the optimal LET value occurs at 100 $\left[\frac{keV}{\mu m}\right]$ because the average distance between ionizing events coincides with the diameter of the DNA double helix; hence, there is a higher probability of causing a double-strand break per particle (see figure 2.2). Even though higher values of LET also produce

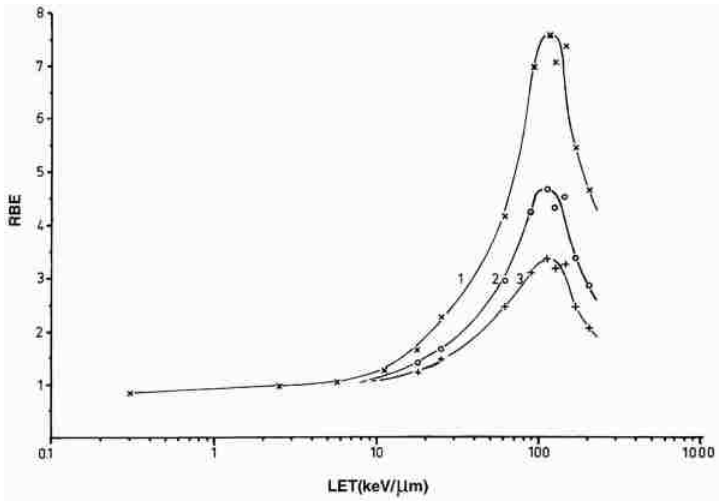

Figure 2.1: RBE as a function of LET [2].

DNA double helix damage, due to a smaller distance among ionizing events, a higher LET (beyond 100 $\left[\frac{keV}{\mu m}\right]$) implies a higher absorbed dose, and since RBE is a ratio of absorbed doses, the RBE decreases.

2.2.7 Water-equivalent path length (WEPL)

The presence in a patient body of many different types of tissues, each with its own physical and chemical properties, is a big challenge for accurate dose calculations. Accurate dose calculations typically require Monte Carlo simulations [28]. In these simulations, random sampling is used to simulate the stochastic interactions and energy depositions of the incident particles through all different types of materials. Accordingly, the accuracy of the results improves with the number of particles simulated. The biggest drawback of Monte Carlo simulations is its long calculation time.

One possibility to overcome this problem is to apply the concept of **water-equivalent path length** (**WEPL**). The intuition behind WEPL is based on the

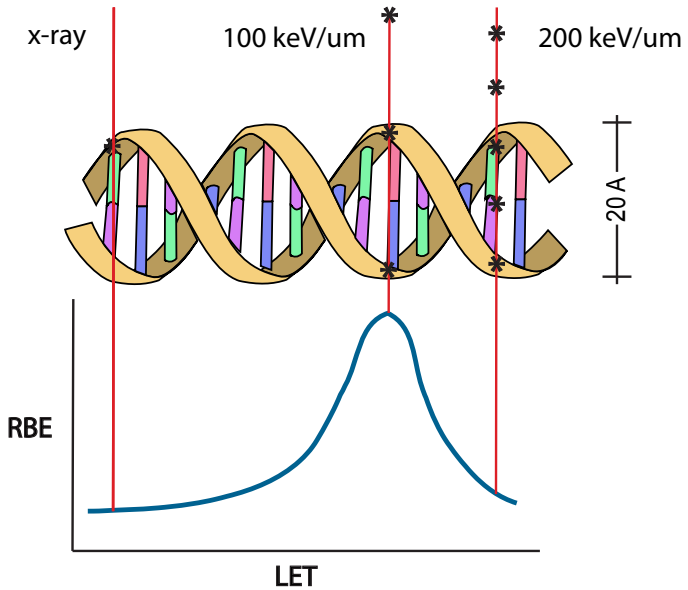

Figure 2.2: DNA Damage. (Based on illustration from [2]).

assumption that when the same particles travel in different media, the basic shape of the dose deposition profile is almost the same except that the range of the particles are different. Thus one only needs to correct the ranges of the particle based on the types of the medium if a dose distribution is already available in water. This gives rise to the concept of water-equivalent path length which is used to correct for inhomogeneities from precomputed dose kernels from water.

Clinically, WEPL is usually given based on the CT numbers or Hounsfield units (i.e., pixel values found on a typical CT scan). Hounsfield units have a direct relationship with electron density, and provide information of the attenuation of a radiation beam while traversing that material [6, 29, 7]. Table 2.1 provides Hounsfield units for different materials and their relative ranges in water.

It is also worthwhile noting that the noisy nature of the CT scan reconstructive method and the uncertainties in the composition of matter, introduce further uncertainties in dose deposition (see section 2.2.2) and linear energy transfer calcula-

Material	**HU**	**Relative range**
Compact bone	1454±35	1.6376±0.018
Muscle	41±5	1.041±0.011
Fat	-108±4	0.943±0.010
Lung	-750±19	0.297±0.010
Spongious bone	262±9	1.095±0.012
Solid water	32±4	1.031±0.011
RW-3	-3±5	1.025±0.011
H-800	-798±11	0.244±0.008
H-500	-485±10	0.468±0.005
H+200	227±10	0.968±0.011
H+400	420±15	1.074±0.012
H+700	792±25	1.216±0.026
H+900	962±35	1.307±0.014
H+1200	1250±65	1.450±0.030
PMMA	138±7	1.165±0.013
Polyethylene	-84±4	0.993±0.011
Alderson phantom	126±5	1.101±0.012
Bovine	1974±21	1.778±0.03
Human bone	1232±265	1.6025±0.001

Table 2.1: Hounsfield Units (HU) and relative ranges in water [6, 7].

tions (see section 2.2.4), since they both depend on the stoppipng power (see section 2.2.3) which is a function of the material the beam interacts with. This nature of Hounsfield units is reflected in table 2.1 where its values are given in terms of a normal distribution by its mean and standard deviation.

Figure 2.3: Lateral cut (CT scan) of a human head.

2.3 Radiation Therapy Treatment Planning

2.3.1 Overview

Modern radiation therapy treatment planning typically involves the following set of steps: patient imaging, target definition (i.e. structure contouring), dose prescription, beam configuration optimization, and quality assurance [30].

Imaging is performed by taking computer tomography scans (CT scans), magnetic resonance imaging (MRI), positron emission tomography (PET) or combinations of these depending on the type of cancer. CT scans are the mostly widely used imaging modalities and can provide anatomical information of the patient (see Figure 2.3). Once these images are obtained, physicians contour the tumor and organs at risk (OARs) as well as prescribe the desired dose.

Modern radiation therapy relies on computer based optimization algorithm and software to generate the beam ocnfiguration for delivering the prescibed treatment. Generally speaking, the optimization model is the following:

- **Patient Representation:** the computational model of a patient is represented by a 3D array of volume pixels (voxels) of some specified resolution (e.g., $1mm \times 1mm \times 1mm$). Each of the voxels is associated with a particular structure such as target or some organ-at-risk.

- **Ideal Dose Distribution:** Aided by the prescription from the physicians, a desired dose distribution can be obtained. There are many ways to represent the ideal dose distribution, we shall assume the ideal dose distribution as a 3D array of dose values in this thesis.

- **Preparation Dose Calculation:** The goal of treatment planning is to select a subset of beams from a set of candidate beams to create the ideal dose distribution. Thus the dose contribution from each candidate beam needs to be calculated before the optimization.

- **Optimization Problem:** Equation 2.10 shows the conceptual optimization problem, where D^* is the ideal dose distribution, D_j is the dose contribution from the $j-$th candidate beam, and t_j is the weighting or beam-on time for the $j-$th beam. The constraint $t_j \geq 0$ reflects that the beam-on time must be non-negative. Thus the goal of the optimization is to find the beam-on times t_j so that the created dose distribution $\sum_j D_j \times t_j$ is as close to D^* as possible. Many metrics can be used to model the "closeness" here, for example the non-negative least square problem [31] as shown in equation 2.10. In certain situations, there maybe additional constraint such as the total beam on time $\sum_j t_j$ must be below a certain threshold t_0. This can be accompanied with additional constraint such as $\sum_j t_j \leq t_0$ and thus resulting in a constrained least square problem [31].

$$\min \left\| \sum_j D_j \times t_j - D^* \right\|_2^2 \quad \text{subject to } t_j \geq 0 \tag{2.10}$$

2.4 Particle Therapy

The therapeutic use of X-rays started as early as their discovery in the 1890s and has become the standard of modern radiation therapy [3]. X-ray depth-dose profile characterizes by a high entrance dose and a long logarithmic decrease dose tail (see figure 2.4). The therapeutic use of heavier charged particles was first proposed by Robert Wilson, in his 1946 paper: "Radiological Use of Fast Protons", where he described the potential benefits of accelerated protons for human radiation therapy [30, 32]. His principal argument was based on the depth dose profile of a proton beam (see figures 2.5), which compared to photon exhibits a low entrance dose, a high dose concentration at some depth (Bragg peak) and a steep dose fall-out after the peak. Since Wilson's early studies, further research has provided better insights into the clinical benefits of charged particles and their higher RBEs compared to photons (see section 2.2.5) [17, 14, 15, 16, 18].

The current most advanced delivery techniques for particle therapy is active scanning. One of the advantages of chaged particles (e.g., protons and carbon ions) over neutral particles (e.g., photons and neutrons) is that the beam direction of a charged particle beam can be oriented with relative ease using a magnetic field. In active scanning particle therapy, the target is first partitioned into layers so that each layer can be reached using the same energy. For each layer, the beam spot (ranging from a few milimeters in diameter to a few centimeters) scans through the layer as shown in Figure 2.6) to deliver the prescribed dose. The planning algoirthms to be discussed in this theis all assume a scanning beam delivery model.

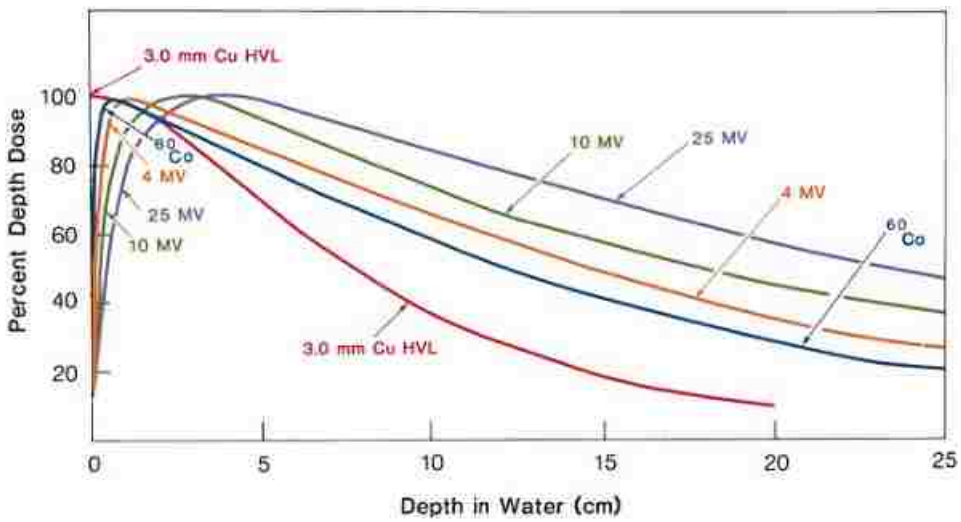

Figure 2.4: Photon beams - depth-dose diagram [3].

For readers interested in the treatment planning and dose calculations of particle therapy, we refer them to the paper by Krämer et. al.: "Treatment planning for heavy-ion radiotherapy: physical beam model and dose optimization", which provides a complete walk-through of dose calculations and the usage of WEPL factors (see section 2.2.7) [33].

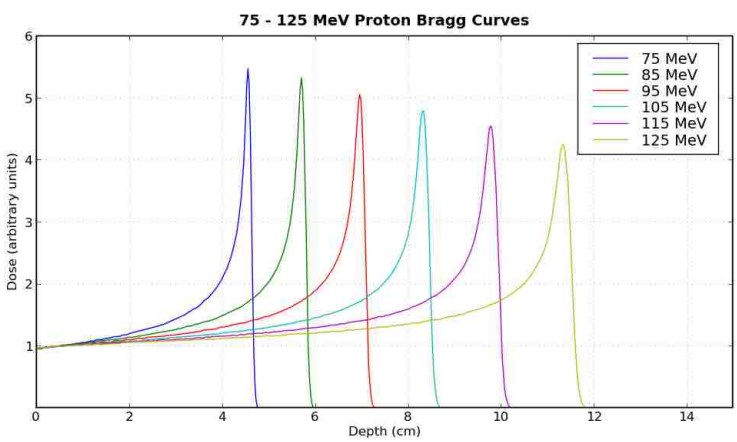

Figure 2.5: Proton beams - depth-dose diagram.

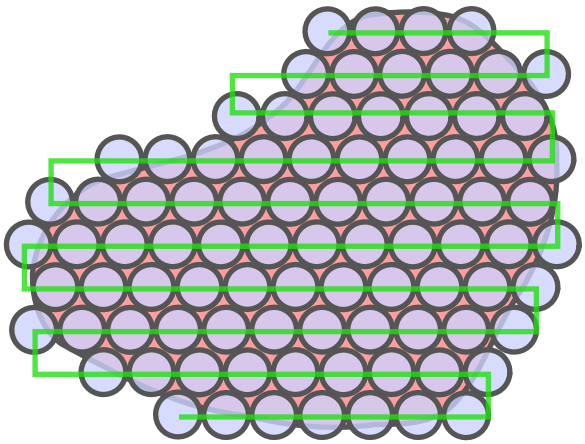

Figure 2.6: Scanning beam therapy: *circles* represent a targeted tumor voxel, and *line connecting circles* represents the scanning path used to "paint" the tumor.

In this thesis, we will use precomputed dose and LET kernels and WEPL for dose calculations. Our precomputed kernels were generated from two well-known Monte Carlo engines: Fluka [34, 35] and GEANT4 [9, 10]. We use Fluka for anti-proton dose kernels and GEANT4 for proton dose and LET kernels. Figures 2.5 and 2.7 show the depth-dose diagrams of proton and anti-proton kernels generated using Fluka[34, 35] from 75 to 125 $[MeV]$ at 10 $[MeV]$ step. Notice how the entrance dose of both particle types is lower and a high dose-volume is concentrated at some depth (Bragg peak). Figure 2.8 shows LET and depth-dose of a proton beam. Notice that the maximum of the LET distribution actually occurs after the Bragg-Peak.

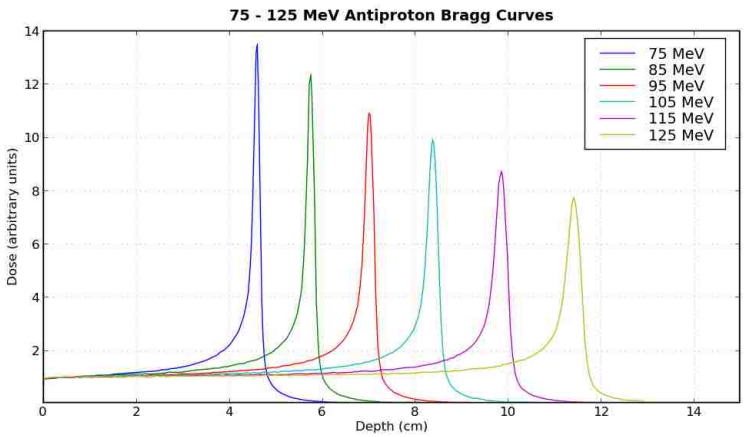

Figure 2.7: Anti-proton therapy - depth dose diagram.

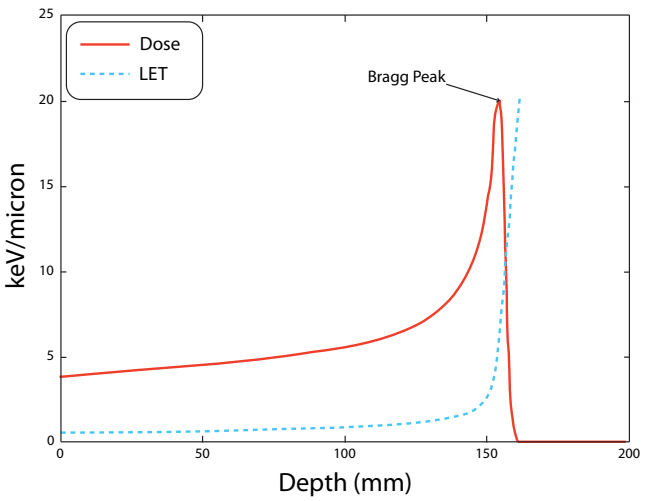

Figure 2.8: LET and depth dose diagram for a 150 $[MeV]$ proton beam.

Chapter 3

Voronoi Partitioning

3.1 Overview

In this thesis, we introduce the concept of a Voronoi diagram to assist planning scanning beam particle therapy. A Voronoi diagram of a set of objects partitions the metric space into cells with one cell per object, such that each cell corresponds to the region closest to its object [36, 37, 38, 39, 4, 40, 41].

Interestingly, the concept of a Voronoi diagram or partitioning is a great deal older than the person it is named after, the Russian mathematician Georgy Voronoy (1868-1908) [39], and has been widely used interdisciplinarily in many fields. Just to name a few, Voronoi diagrams have been used in astronomy, anthropology, biology, chemistry, geography, physics, physiology, statistics, machine learning, and robotics. The first studies using this type of space partitions were performed by Descartes in the 16^{th} century while showing the disposition of matter in the solar system (see figure 3.1) [39, 4, 40]. For example, in figures 3.2 and 3.3 one can see Voronoi partitions using Euclidean distance of different objects such as for a set of points (see figure 3.2), line segments, polygons (see figure 3.3). Interestingly, Voronoi diagrams also

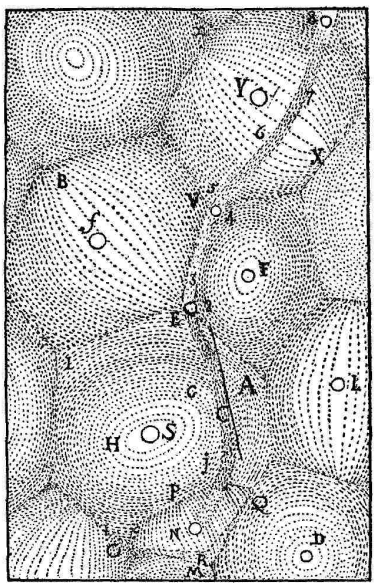

Figure 3.1: Descartes' disposition of matter in the solar system [4].

occur in nature such as in the root systems of plants and skin patterns on a giraffe (see figure 3.4).

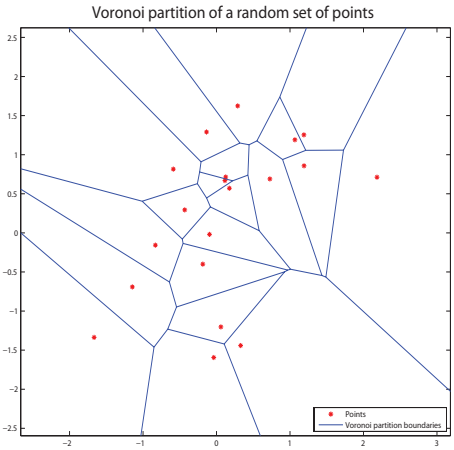

Figure 3.2: Voronoi diagram of a random set of points in $\mathbb{R}^2$.

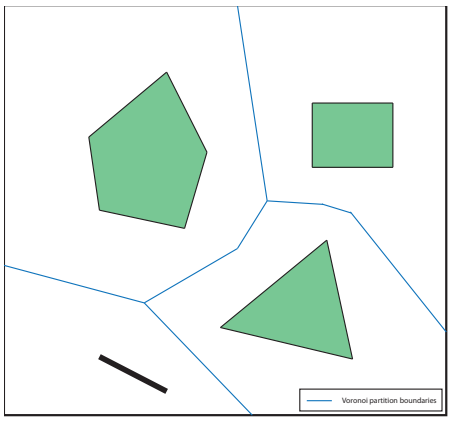

Figure 3.3: Voronoi diagram of different geometrical objects in $\mathbb{R}^2$.

3.2 Definitions

It is a common practice to start the study of Voronoi partitioning stating the two-dimensional version of the problem and then generalizing to its n-dimensional version. Nonetheless, the following formulation of Voronoi partitioning tries to be as general as possible so that it can be easily stated in any dimensionality.

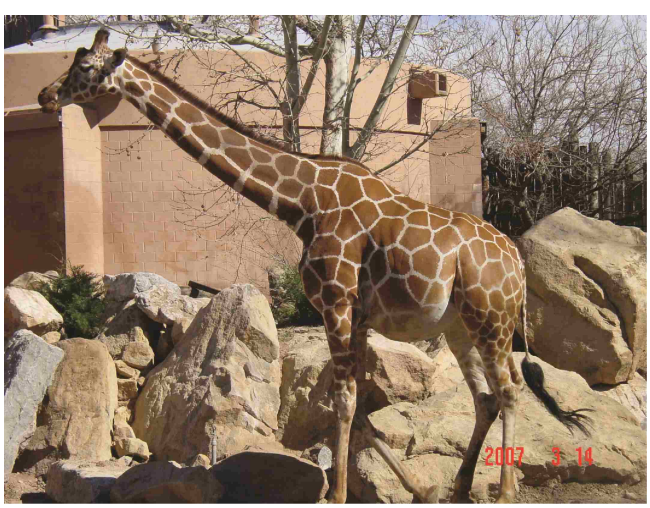

Figure 3.4: Voronoi diagram in nature: the giraffe's skin pattern is a planar Voronoi partition.

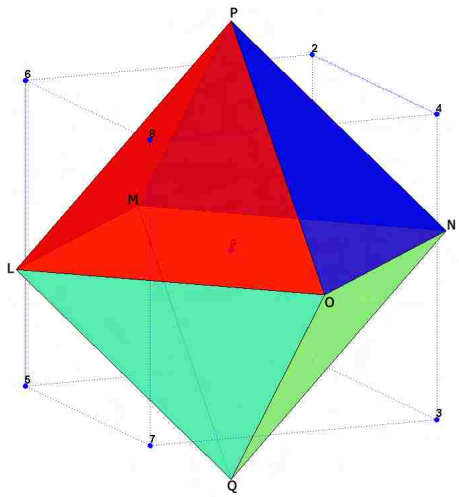

Figure 3.5: Voronoi diagram of nine points placed on the edges of a cube and its center in $\mathbb{R}^3$.

Let, $O = \{o_1, o_2, ..., o_n\}$ be a collection of n objects in some set S with a distance function defined $(distance_s(o_i, o_j))$, $\mathbb{N}$ the set of natural numbers, and $\mathbb{R}$ the set of real numbers. Then, a Voronoi partition is a decomposition of S into *Voronoi cells* $V = \{V(o_1), V(o_2), ..., V(o_n)\}$, such that $S = \bigcup_{i=2}^{n} V(o_i)$ and $V(o_i) = \{o | distance(o, o_i) \leq distance(o, o_j)\ for\ j \neq i\}$.

When the set O is the set of points in the real plane, $\mathbb{R} \times \mathbb{R}$ or $\mathbb{R}^2$, with euclidean metric,

$$\forall i, j\ i \neq j\ distance_S(o_i, o_j) = \sqrt{\big(o_j(1) - o_i(1)\big)^2 + \big(o_j(2) - o_i(2)\big)^2}$$

where, $o_i(1)$ and $o_i(2)$ stand for the x- the y-coordinates of point o_i then the Voronoi partition V is a planar graph [39], where each face or Voronoi cell is a polygon as shown in Figure 3.2.

When the set O is the set of points in the three-dimensional real space, $\mathbb{R} \times \mathbb{R} \times \mathbb{R}$

or $\mathbb{R}^3$, with euclidean metric:

$$\forall i, j \; i \neq j$$

$$distance_S(o_i, o_j) = \sqrt{\big(o_j(1) - o_i(1)\big)^2 + \big(o_j(2) - o_i(2)\big)^2 + \big(o_j(3) - o_i(3)\big)^2}$$

where, $o_i(1)$, $o_i(2)$, and $o_i(3)$ stand for the x-, y-, and z-coordinates of a point o_i then the Voronoi partition is a set of polyhedrons as shown in Figure 3.5.

In addition, the set of objects O can be considered as a multi-set where inhomogeneous elements are part of it, for example figure 3.3 shows a Voronoi partitioning of geometrical objects such as lines and polygons of different sides. The key is that these objects have to be representable within the metric space such that $distance_S(o_i, o_j)$ is defined for inhomogeneous objects. Hence in the case of figure 3.3, $distance_S$ was defined using euclidean distance that measures the distance from a point to a line and generalizing it for a set of lines.

3.3 Complexity

On a geometric setting, a Voronoi diagram consists of a collection of regions, where each region is defined by a set of faces, edges and vertices. The number of such faces, edges, and vertices is referred to as the complexity of the Voronoi partition. This complexity is also a lower bound of how long it takes to generate a Voronoi partition.

Shamos [42] in his Ph.D. dissertation proved that computing the Voronoi partitioning of a set of n points in $\mathbb{R}^2$ is at least as difficult as sorting n real numbers, which is a problem that requires $\Theta(n \log n)$ [4]. Although, a technique known as bucket-sort has been proved to take expected linear time [43] , $O(n)$, to sort n elements has also been used to speed-up some of the algorithms that compute planar

Voronoi diagrams under some special conditions [39].

In the case of higher-dimensional Voronoi diagrams, the complexity of the Voronoi diagram increases with the dimensionality according to the number of $k-$faces in the diagram which is in the order of $\mathrm{O}\left(n^{min\{m+1-k,\lceil m/2\rceil\}}\right)$ for n generators in m dimensions and $0 \leq k \leq m$ [44, 37]. In the three-dimensional case, the number of vertices in the Voronoi diagram is bounded by $\mathrm{O}(n^2)$. This fact implies that the lower bound of any algorithm that constructs a Voronoi diagram in three dimensions is $\mathrm{O}(n^2)$ [39, 37].

3.4 Algorithms

Many algorithms have been developed to calculate the planar Voronoi diagram of a set of n points [45, 46, 47, 48] and later generalized to handle higher-dimensions. In this section we describe the general strategy of three traditional optimal algorithms to compute the Voronoi partition of a set of points in the plane as well as (some of them) in three-dimensions for the Euclidean distance. In addition, we discuss a hardware-aided approach to approximate generalized Voronoi diagrams using graphics processing units (GPU) which are specialized hardware processors that compute vectorized operations using fast algorithms implemented at hardware-level.

3.4.1 Incremental method

The basic idea under this algorithm is to insert a generator point o_l into a Voronoi diagram and pay the price of updating the Voronoi cell of the o_l^{th} face added to the diagram. Hence, a potential solution is to search for the closest o_j and modify its Voronoi cell to consider the new boundaries imposed by the presence of the o_l genera-

tor point. This operation can be calculated by exhaustive search $\min_j distance_S(o_l, o_j)$ for all $2 \leq j \leq l-1$. This approach has a total complexity of $\mathrm{O}(n^2)$, though smarter data structures can be used to reduce its running time to a worst-case of $\mathrm{O}(n \log n)$ and average runtime $\mathrm{O}(n)$ [45, 39, 37]. For higher dimensionality this approach takes $\mathrm{O}\left(n^{\lceil \frac{m}{2} \rceil}\right)$, where m is the dimensionality of the metric space S [37].

3.4.2 Divide-and-conquer method

As in any other divide-and-conquer algorithm, this algorithm divides the input in smaller pieces and recursively breaks down the construction of the Voronoi diagram into simpler subproblems and then pays the price of merging the solutions of these subproblems. Hence, if the input set is of cardinality n and $n > 3$, this algorithm divides the input in $O_l = \left\{o_i \mid 1 \leq i \leq \lceil \frac{n}{2} \rceil\right\}$ and $O_r = \left\{o_j \mid \lceil \frac{n}{2} \rceil \leq j \leq n\right\}$, then recursively calls to solve for the Voronoi partition on O_l and on O_r, merges the solutions V_l and V_r in V, then returns V. Since, the only operation that does not involve a constant or linear time is the merging step, this algorithm is bounded by how fast two Voronoi partitions of size roughly $\frac{n}{2}$ can be merged. As shown in [39] the merging process can be calculated by finding the *lower common support* of the *convex hull* of O_l and O_r which can be done efficiently in $\mathrm{O}(n)$ time. This results in the recurrence relation $T(n) = 2T\left(\frac{n}{2}\right) + \mathrm{O}(n)$, where $T(n)$ is the running time of this algorithm, that yields to a total total worst-case running-time of $\mathrm{O}(n \log n)$.

3.4.3 Plane sweep method

Plane sweep algorithms are elegant computational geometry algorithms that use a geometric structure usually a plane or line (conventionally perpendicular to an axis in a space) to sweep the space left-to-right while computing a desired output. The beauty on plane sweep methods lies on the ability to maintain the desired partial

solution of the problem up to the place the sweep plane is located. In particular, in the two-dimensional Voronoi diagram calculation requires to keep a conic data structure to maintain track of the Voronoi boundaries that are yet to be discovered to the right of the sweep line. This sweep line algorithm has a worst-case running time of $O(n \log n)$ [46, 39].

3.4.4 Discrete Voronoi diagram

In a discrete setup, Voronoi diagrams can be obtained using some novel methods such as the one proposed by *Hoff et. al* in [48] where they propose to use graphical processing units (GPUs) to speed up the process of obtaining planar and volumetric tessellations. In their proposed methods, they rely on this specialized hardware to calculate (using interpolation) and impose (using the Z-buffer) an approximate distance mesh on top of their geometry and compare (using the Z-buffer depth comparison) which set of pixels or voxels are closer to the each of the Voronoi generators. Finally, they use polygon scan-conversion in order to obtain the Voronoi cell boundaries.

3.5 Our model

The formulation of our partitioning problem consists on a given set of beam directions, O, and a set of voxels P, whose subsets T and F, $T \subset P$ and $F \subset P$, represent tumor voxels and skin peripheral voxels of the patient respectively, in the Euclidean space, S, with possible weighted Euclidean distance and obstacles. We want to specify for all $t_i \in T$, $f_i \in F$ along all $o_k \in O$ directions the closest set of voxels to each direction using the distance $distance_S(t_i^k, f_j^k)$. Figure 3.6 a two-dimensional CT-scan Voronoi diagram of a brain tumor for two given angles (30° and 150°).

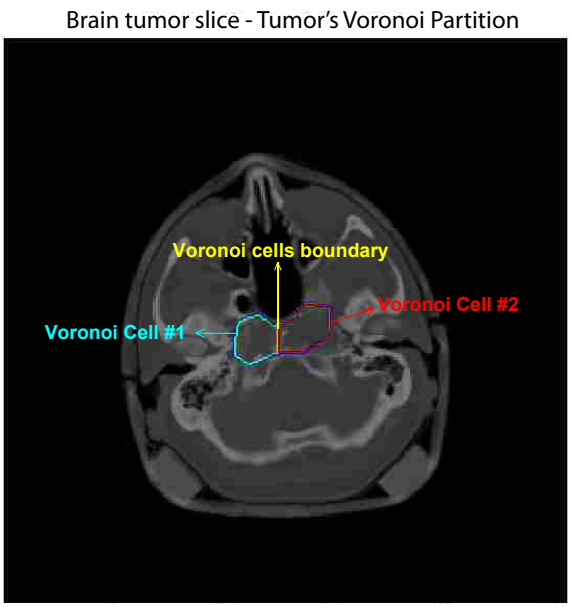

Figure 3.6: Voronoi diagram of a brain tumor for two beam angles.

Chapter 4

Treatment Planning System Prototype

4.1 Overview

In section 2.3 we introduced the concept of a treatment planning system (TPS) and some of the tasks that a TPS is expected to perform. In this thesis, we developed a TPS prototype taht is capable of (1) importing a representation of a patient (e.g., raw CT images, contoured anatomies, etc), beam configurations (e.g., beam angles, energies, and etc), and dose prescriptions, (2) performing kernel based dose and LET calculations, (3) optimizing a given objective function using non-negative least squares solver, and (4) outputting the final dose and LET distributions and summaries such as DVH and LVH plots (see below for more details), and beam configuration (angle, targeted tumor voxel coordinates) for the treatment plan. Figure 4.1 shows in summary the components and tasks developed in this thesis as well as the optimization module that is taken from [5]. The components developed as part of this thesis are described in detail in the following sections.

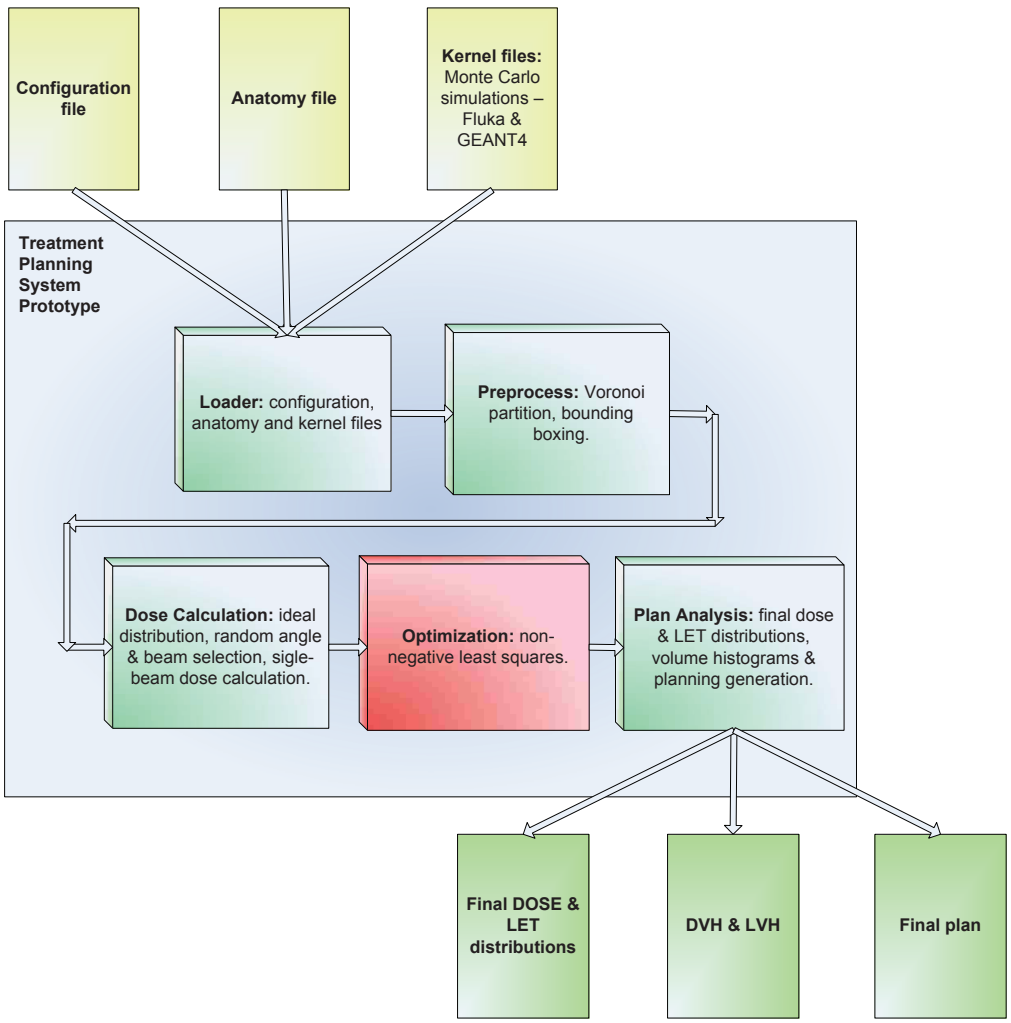

Figure 4.1: Treatment planning system prototype. *In yellow:* input files (configuration, anatomy and kernel files). *In blue:* treatment planning system prototype components. *In dark green:* components implemented as part of this thesis. *In red:* optimization component (non-negative least squares) developed by Chen [5]. *In light green:* output files (dose and LET distributions, volume histograms and final treatment plan).

4.2 Modules

In this section, we discuss the different components (modules) implemented as part of this thesis as well as some of the coding challenges for future work. The treatment planning system prototype has been implemented using C programming language, since it allows low-level and fast interaction with commodity operating systems such as Linux and Windows. Therefore, the coding has been done carefully so that the program runs on both UNIX (Linux) and Windows platforms.

4.2.1 Loader

This component is in charge of reading and interpreting all files in the system. We use a configuration file for specifying the anatomy and kernel files as well as providing initial values for the memory management process that is performed throughout the execution of the whole system.

The anatomy file is used to describe the contoured volumes obtained from a CT-scan as well as the prescribed ideal dose and its tolerance levels per anatomical structure. Internally, we differentiate four hard-coded structure types: air=0, tissue=1, target=2 and sensitive=3. This can be easily extended to accommodate a finer tissue classification.

Furthermore, a water-equivalent path length anatomy mask containing WEPL factors for each voxel is also implemented in the system for dose calculation under inhomogeneous medium (see section 2.2.7 table 2.1 for more details). This mask is the result of a linear interpolation from the CT numbers read and mapped to WEPL-factors and it is obtained by a MATLAB script described in section 4.3.

The kernel files are represented using a linked list data structure which is sorted by the beam's Bragg Peak depth. At this point, our kernels are represented using polar

coordinates along the beam direction with a dimension of 300×41 at a resolution of $1[mm] \times 1[mm]$. We used a total of 21 kernels from $75[MeV]$ to $175[MeV]$ at a resolution of $5[MeV]$. One could expect that with increased resolution and reduced energy step, accesing the kernels may become a bottle neck. Thus as part of our future work, we are considering using a file cache scheme to only load the kernels that has been requested.

4.2.2 Pre-process

According to the flags loaded from the configuration file, this module decides whether or not to perform a Voronoi partition from the provided anatomy. In the current version, we provide a straight-forward approach of calculating a Voronoi partition since we are only dealing with a small set of treatment beam angles. Although this algorithm does not scales properly in the presence of many beam angles and a higher voxel resolution, the current algorithm implemented is not affecting the performance of the complete system prototype. Nonetheless in the future, we plan exploring incremental algorithms or GPU-based algorithms for faster calculations.

In order to perform a Voronoi partition of a set of voxels with inhomogeneities, we developed a simple ray-tracing algorithm, which for a given beam angle and a target voxel coordinates returns a set of voxels and the total distance traversed by the beam inside each one. Then scaling the total distance in this inhomogeneous environment, it is just a matter of adding up each individual voxel distance multiplied by its medium scaling (WEPL) factor. In addition, this prototype allows to calculate Voronoi partitions using the euclidean distance in two scenarios: distance from targeted tumor voxel to surface, and distance from targeted tumor voxel to tumor's surface.

Finally, a bounding box is imposed over the tumor and organs at risk within a safe

boundary predefine in our configuration. This bounding box allows the optimization algorithm to consider a smaller subset of voxels to tune for the final beams to be used during the actual treatment.

4.2.3 Dose Calculation

As mentioned in section 4.2.2, we developed a ray-tracing algorithm that is able to return the beam path from the center of the targeted tumor voxel to the surface of the patient along a given beam direction. Using this information, we scale the distance if it is the case of an inhomogeneous medium, and according to the distance we select the closest beam that can deposit its Bragg peak inside the targeted tumor voxel. Depending on the pre-process, if a Voronoi partition was performed a beam direction is fixed by voxel, then our random beam selection algorithm selects whether or not to use a voxel as a target. In the case no partition was imposed, our random angle and beam selection algorithm selects an angle with equal likelihood among the beam directions provided and also chooses whether or not to use a voxel as a target.

Once we select the beam directions and energies, we perform dose calculations per each beam. In addition, we generate the ideal dose distribution and execute the non-negative least squares routines to filter out those beams that do not contribute to the final dose distribution. This process is done iteratively in order to avoid small contributions (beam weights less than a threshold) of some beams.

Nonetheless, there is one known issue with our implementation. Using the current ray-tracing algorithm for performing dose calculation implies to perform multiple distance calculations: one to know the depth where to place the Bragg peak, and one per every other voxel to know its depth and lateral off-center distance. This extreme ray-tracing environment provokes a considerably slow-down in performance while performing dose calculation. Hence in order to get around this problem, we

use our specialized ray-tracing algorithm to calculate a precise depth where to place the Bragg peak and we estimate the lateral off-center distance by calculating the distance from every other voxel to the vector defined from the surface to the targeted tumor voxel (see figure 4.2). Although we understand that it is not a very precise calculation, in practice this is often done since the lateral spread of a beam is considerably smaller than the depth it traverses and the size of the volume treated. Nonetheless, if a more accurate dose calculation is desired it is part of our future work to develop or try faster ray-tracing algorithms. One alternative, that could help speeding-up this process is to increase data locality by providing a cache system to save the paths a beam traverses in one direction and reuse them for all the beams interacting in the same or in its opposite direction.

4.2.4 Optimization

In our previous section (see section 4.2.3), we described how dose calculation is performed to feed our optimization routine. In particular, we make a function call to the non-negative least squares solver [31] implemented by [5] passing a set of pointers that are reserved in our main program and is filled with the data we want to optimize. The beam interactions (dose calculation per beam), the ideal dose distribution, as well as an array to place the beams weighting is passed to this function and iteratively run until no more beams are filtered by our beam contribution threshold. Furthermore, it is worth mentioning that a small bug on the non-negative least squares solver implementation was fixed in order to address memory beyond $2^{32} - 1$ bytes. In our simulations we have used the multi-threading float precision version of this non-negative least squares solver.

4.2.5 Plan Analysis

Finally, once we have our final beam weighting factors, we preform a final dose calculation and during this time we also calculate the LET distribution using equation 2.8. Since this process finishes, dose and LET distributions are stored in a text file. From these final distributions, our volume histogram algorithms count the number of voxels within a dose or LET value and produce the DVH and LVH text files (see the glossary for the definition of DVH and LVH).

In addition, a file is produced containing the information of the beam used (energy), its direction, its weighting factor and the voxel coordinates it targeted. This final file is the source used to compare two different treatments in terms of energy modulation reduction.

4.3 Additional tools

In order to visualize the results of our simulations, we have developed several MATLAB scripts to load and plot dose and LET distributions, as well as, load and plot volume histograms. A brief description of the most important tools are described in the following list:

- **Distributions plotter:** this script loads a dose or LET distribution file and shows its iso-dose or iso-LET map per slice, furthermore two 2D images are produced showing dose in green over the phantom in blue, and LET in red over the phantom in blue.
- **Tumor contouring:** using MATLAB contouring functions we automatized a procedure to manually do tumor contouring for producing the phantoms used on this thesis.

- **Volume histograms plotter and verifier:** this script reads a DVH or LVH file and produces a plot showing the histogram. It can also produce a DVH or LVH from an existing dose or LET distribution.

- **Ray-tracing algorithm:** this script was implemented as a proof-of-concept of the algorithm used for ray-tracing in this thesis. It has allowed to create Voronoi partition masks to avoid calculating Voronoi partitions every time we changed the conditions of our simulations.

- **Kernel interpolator:** this script has been used to create new kernel information as proof-of-concept whenever we lacked for some beam energy in order to avoid going through a complete Monte Carlo simulation on Fluka or GEANT4.

- **Phantom generator:** this script was used to create the C-shaped phantom used as part of the simulations proposed in this thesis.

- **Kernel configuration helper:** this tool was implemented using C#.Net and it has been used to automatically create the kernel index file which contains the paths of all kernel files used by the treatment planning system prototype.

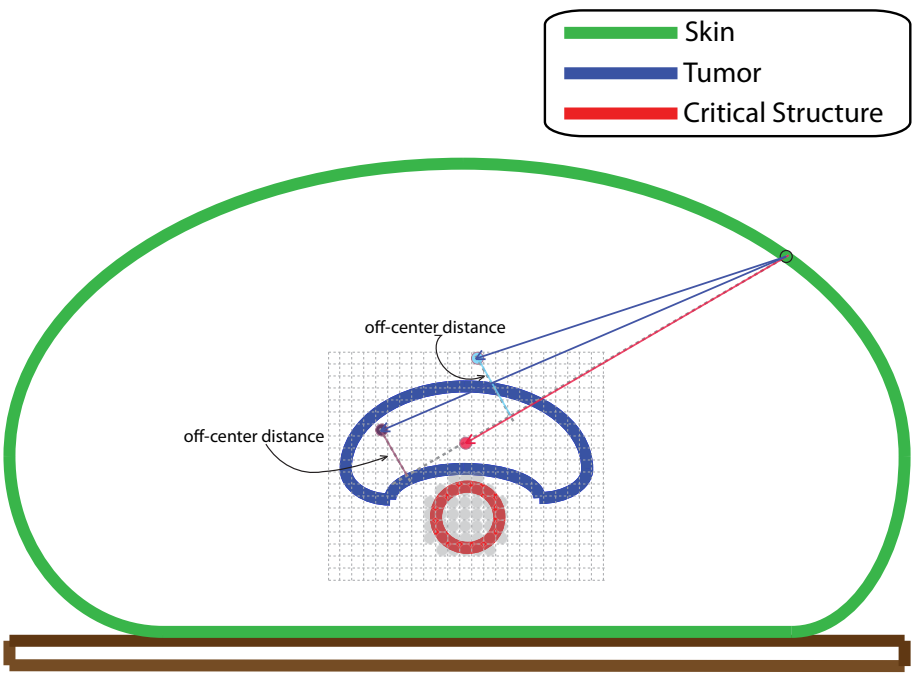

Figure 4.2: Off-center distance estimation through the projection of two vectors.

Chapter 5

Applications

5.1 Beam Energy Modulation Reduction

5.1.1 Problem description

Given a set of beam directions, the energy modulation reduction problem aims to find a beam configuration to create a dose distribution as close to the ideal, while in the meantime reducing the number of energy changes.

5.1.2 Motivation

In scanning beam therapy, beams are selected to target tumor voxels with their highest dose (Bragg Peak). As a consequence of the Bragg Peak's localization is a function of the beam energy, in scanning beam therapy has to take into account the time it takes to modulate energies to target deeper voxels (see figure 5.1). Since, changing beam energies requires an undesirable extra treatment time, a high quality treatment plan with minimum number of energy changes is desirable.

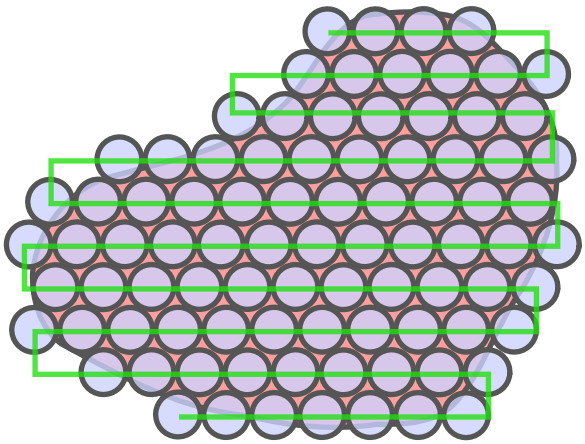

Figure 5.1: Scanning beam therapy: *circles* represent a targeted tumor voxel, and *line connecting circles* represents the scanning path used to "paint" the tumor.

5.1.3 Proposed Solution

Our new planning algorithm mainly uses 2 key steps: Voronoi partition of the patient anatomy and plan optimization based on Voronoi partitions.

Voronoi Partition: A Voronoi partitioning of the targeted tumor for the given beam angles is first calculated, where each Voronoi cell contains the portion of the targeted tumor closest to its beam. Here by closest, we mean to be able to hit a target from a beam angle with minimum penetration of normal tissues and no penetration of critical structures. Since in scanning beam particle therapy, the source can be viewed as a set of parallel beams, each beam is modeled as a plane in 3D space perpendicular to the beam direction and passing through the beam source. In the Voronoi partition, the objects are basically these 3D planes, each representing a beam angle.

Figure 5.2 illustrates this model in coplanar beams. In this example, we are look-

ing at a 2D slice of a 3D C-shaped tumor, where each beam direction is modeled as a straight line perpendicular to the beam direction. The targeted tumor is partitioned into 3 Voronoi cells. When critical structures are present between the beam source and the targeted tumor, they are modeled as obstacles in the Voronoi partition to either avoid being penetrated by a beam or minimize the beam path going through them. It is also worthwhile to note that Figure 5.2 mainly serves as illustrative purpose. The actual implemented algorithm also works for non-coplanar beams and with arbitrary arrangement of critical structures.

Given a set O of potential beam directions whose cardinality is n, (i.e. $|O| = n$), a set of voxels corresponding to a tumor of cardinality $|P| = l$ the objective function to minimize is as shown in equation 5.1, where $distance_S\left(p_i^k, p_j^k\right)$ stands for a function that calculates the distance traversed in a beam direction k from its surface voxel i to its targeted tumor voxel j.

$$\min\left(\sum_{k=0}^{n}\sum_{i=0}^{l} distance_S\left(p_i^k, p_j^k\right)\right) \tag{5.1}$$

Notice that the solution of equation 5.1 can be calculated by exhaustive search in $\Theta\left(n * p\right)$.

Optimization: During optimization, each beam only treats the tumor region within its Voronoi cell. The final dose distribution is optimized using a combination of randomization and non-negative least squares algorithm. In our modeling, a beam of heavy charged particles is viewed as a high dose volume (called a "shot") localized in its Bragg Peak region, and the strategy of treatment planning is to route this shot to cover a target volume. The key steps of our optimization are: (1) Geometric and randomized techniques to select a collection of potential shots based on pre-computed kernels of different energies. (2) Constrained least square optimization

to filter out the final shots. (3) "Traveling salesman" algorithm to route the final shots. (4) Interpolation of the route, performing an accurate dose calculation for each interpolation point. (5) Constrained least square optimization to calculate the dwelling time of each interpolation point.

5.1.4 Results

We created a C-shaped phantom (see figure 5.2) which has been preprocessed using the modules developed in our treatment planning system prototype (see section 4) in order to get its voronoi partitioning for a set of three angles (direction 1: 180°, direction 2: 0° and, direction 3: 90°). In addition, we developed some MATLAB scripts to plot our results.

Figure 5.2 shows the phantom and the setup used for this optimization problem. In addition, we decided to compare this algorithm using two different radiation therapies: proton therapy and anti-proton therapy. Although, anti-proton therapy is not yet used in clinics we explore some of its potential benefits and properties.

Figure 5.3 shows an iso-contour dose conformity comparison map of the different treatment plans simulated. Proton and anti-proton therapies are shown in two scenarios, one when the Voronoi partitioning of the phantom was calculated and the other where no partitioning was calculated. In the second approach, we let the general randomized algorithm implemented as part of the treatment planning prototype to choose from the list of possible beam angles which to use to target a tumor voxel. In terms of radiation therapies, a conformal dose is obtained; although, anti-proton therapy delivers a higher dose to the critical structure (see figures 5.4 and 5.12).

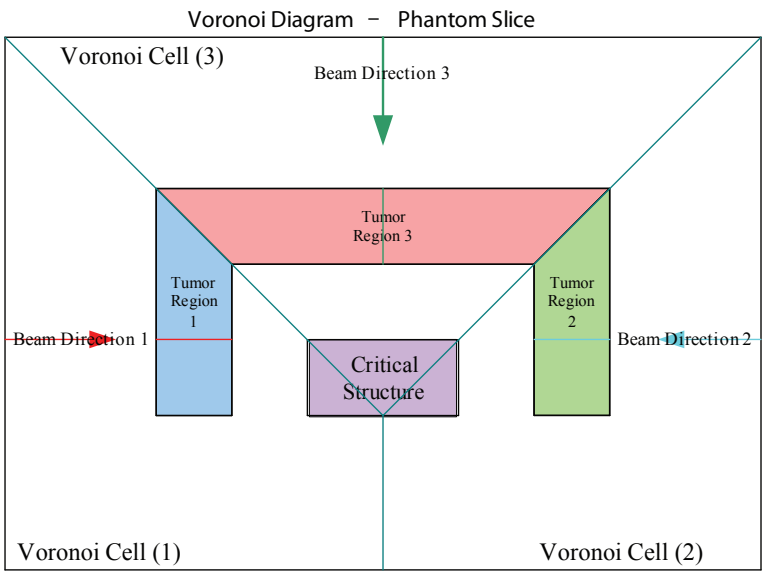

Figure 5.2: Voronoi partition of a C-shaped phantom for three orthogonal angles given.

In addition, we add a general comparison figure that provides some insights of the benefits of each type of radiation therapy (see figure 5.12). Anti-proton therapy allows for a lower entrance dose compared to proton therapy; on the other hand, proton therapy allows for a sharper dose fall-off protecting the critical structure from receiving a higher dose than the one in anti-proton therapy. Furthermore, despite of the trade-offs of each therapy high quality treatment plans are achieved.

Finally, tables 5.1 and 5.2 show the savings in the number of energies needed to "paint" the phantom. In both cases, using Voronoi partitions to select which angle to use before running the non-negative least squares optimization module allows for savings in 70% of the energies compared to a randomize selection of beam angles.

Beam direction	**No E.M.R.**	**E.M.R.**
1	28	7
2	22	8
3	27	8
Total	77	23
Savings		**70.13%**

Table 5.1: Proton therapy results comparison: Energy modulation reduction vs. no energy modulation reduction.

Beam direction	**No E.M.R**	**E.M.R**
1	31	8
2	21	8
3	30	8
Total	82	24
Savings		**70.73%**

Table 5.2: Anti-proton therapy results comparison: Energy modulation reduction vs. no energy modulation reduction.

5.2 Simultaneous Dose & LET painting

5.2.1 Problem description

Given a set of beam directions, the simultaneous dose & LET painting aims to find a beam configuration that simultaneously produce a high quality dose treatment plan with a high concentration of LET inside the tumor avoiding delivering high LET to organs-at-risk and healthy tissues.

5.2.2 Motivation

In section 2.2.6, we described LET and its relationship with RBE. Specifically, the fact that a higher LET (up to 100 $\left[\frac{keV}{\mu m}\right]$) produces DNA double helix damage, which

may disrupt cell's reproductive abilities and eventually provoke its death. Hence, a treatment planning algorithm that delivers a high dose and high LET into the tumor avoiding organs-at-risk is desired.

5.2.3 Proposed Solution

Our new planning algorithm mainly uses 2 key steps: Voronoi partition of the patient anatomy and plan optimization based on Voronoi partitions.

Voronoi Partition: A Voronoi partition of the targeted tumor for the given angles is first calculated, where each Voronoi cell contains a portion of the targeted tumor according to the metric in use. We propose the use of two metrics, one that measures the closest beam to a tumor voxel (see definition of $distance_S\left(p_i^k, p_j^k\right)$ in section 5.1.3) and another that measures the closest beam to a tumor voxel where $distance_S\left(p_i^k, s_j^k\right)$ where s_j^k is the outermost tumor voxel from tumor voxel p_i^k along the k^{th} beam angle direction.

We explore LET function geometrical properties (see figure 5.6) and realize that the highest LET region is pushed further from its Bragg Peak along the beam direction. Hence, we hypothesized that overlapping several "opposing" beams would let to a higher LET region inside the tumor where beams encounter at a virtual boundary inside the tumor (see figures 5.7 and 5.8). Note that virtual boundaries can be imposed by using different metrics that divide the tumor internally. Figure 5.7 shows our hypothesis of using two angles, and figure 5.8 of using three angles.

Optimization: During optimization, each beam only treats the tumor region within its Voronoi cell. The LET distribution is calculated using the equation for dose averaged LET (see 2.8). The final dose distribution is optimized using a combination of randomization and non-negative least squares algorithm as previously described in section 5.1.3.

5.2.4 Results

Our first empirical test consisted on using 30° and 150° beam angles which are angles that have been calculated by an angle selection algorithm which minimizes the inhomogeneities through the beam path. We assume this treatment plan as our starting point and perform dose and LET calculations for two different treatment plans: one that calculates the voronoi partition using our first metric and the second without partitioning. Figure 5.9 shows dose and LET distributions of these plans. It is worth mentioning that a normal treatment plan pushes the higher LET regions outside the tumor, and in this specific case, high LET regions are pushed onto one critical structure (the brain stem). On the other hand, despite the use of Voronoi partitions it is noticeable that a higher LET region is localized unfortunately very close to the brain stem although higher LET values are still deposited inside the tumor.

Dose and LET volume histograms were calculated to confirm the visual content of figure 5.9, these histograms are shown in figure 5.10. Since, the highest LET region is pushed close to the brain stem, we decided to test partitioning the tumor using our second metric using three angles to avoid this high LET concentration close to the brain stem. Figure 5.11 shows the result of using voronoi partitions using 90°, 210° & 330° beam angles. Similarly, Dose and LET volume histograms were calculated as shown in figure 5.12.

It is noticeable that a very high LET can be obtained and targeted inside the tumor while delivering very low LET to critical structures using a Voronoi partition that imposes more complex internal boundaries inside the tumor. DVH and LVH confirm our previous observation.

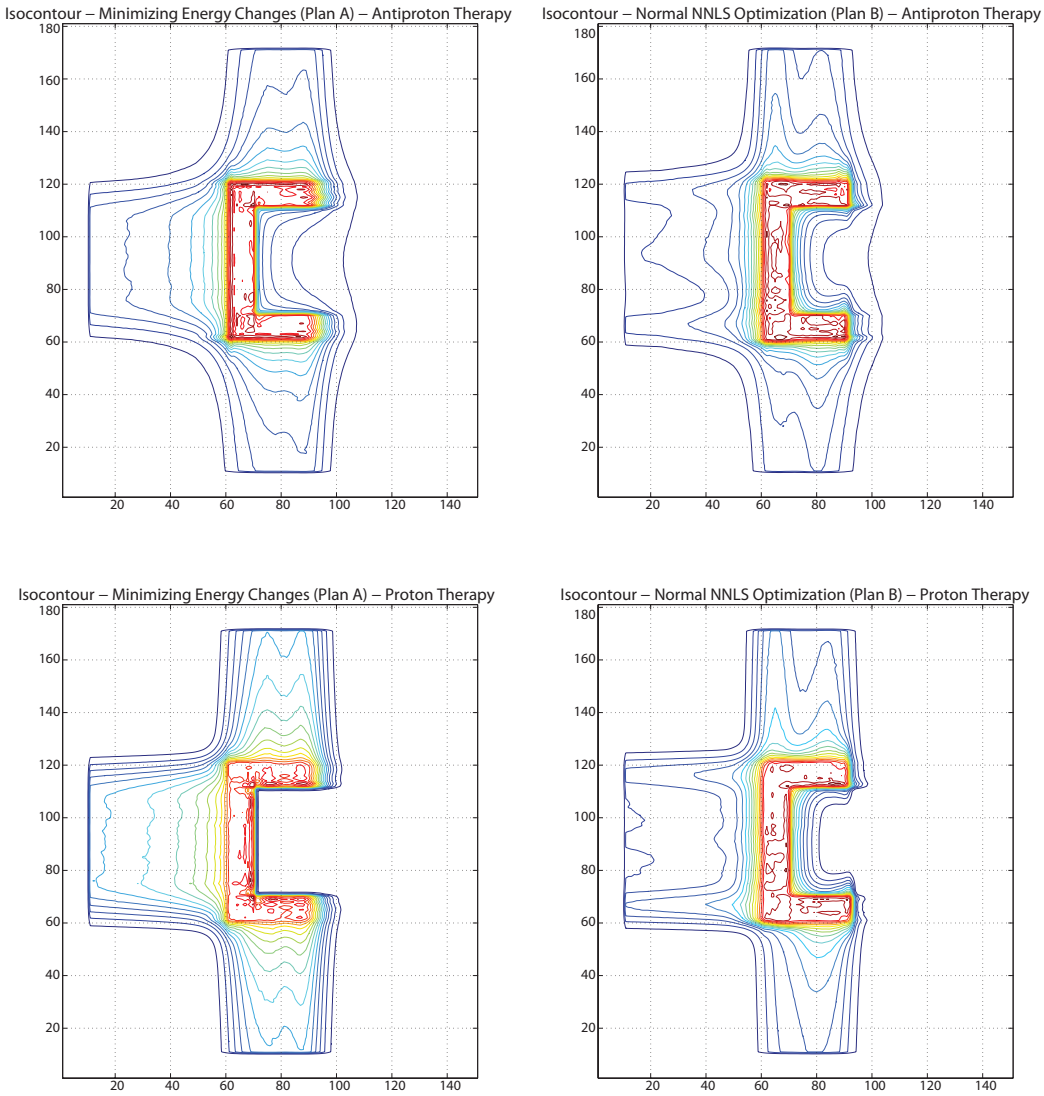

Figure 5.3: Proton and anti-proton dose distributions for energy modulation reduction and no energy modulation reduction. *Top left (Plan A):* iso-contour dose distribution using Voronoi partitioning for anti-proton therapy. *Top right (Plan B):* iso-contour dose distribution using normal optimization without partitioning for anti-proton therapy. *Bottom left (Plan A):* iso-contour dose distribution using Voronoi partitioning for proton therapy. *Bottom right (Plan B):* iso-contour dose distribution using normal optimization without partitioning for proton therapy.

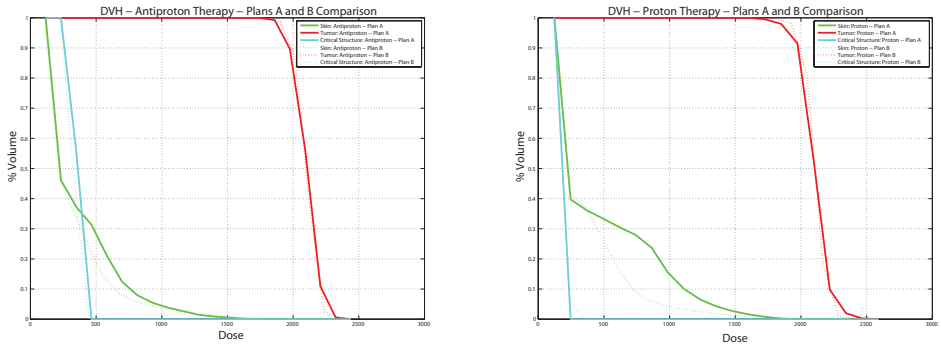

Figure 5.4: Proton and anti-proton DVH comparisons for energy modulation reduction and no energy modulation reduction. *Left:* Plan A vs Plan B for anti-proton therapy. *Right:* Plan A vs Plan B for proton therapy.

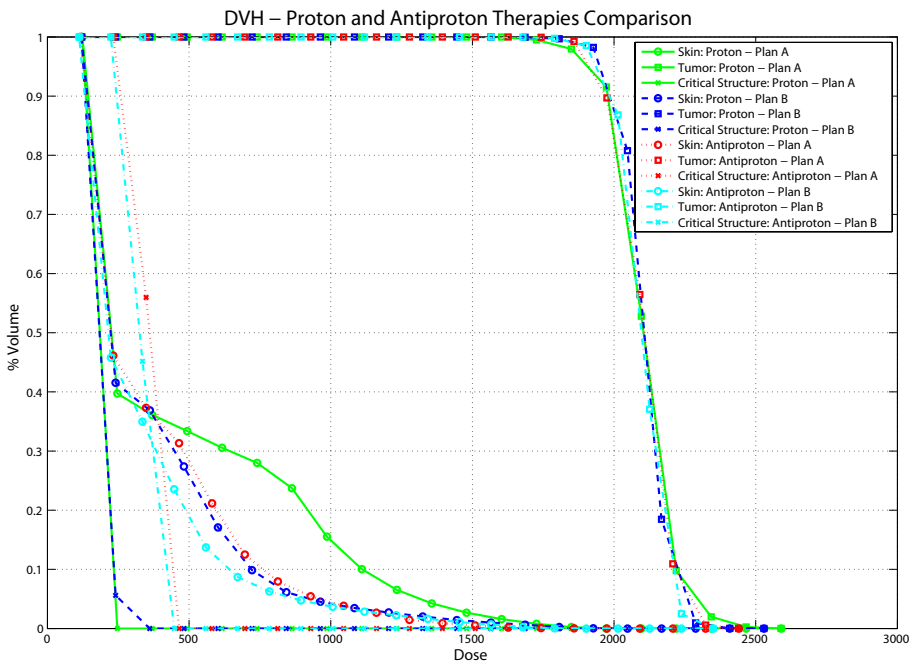

Figure 5.5: Proton and anti-proton DVH general comparison.

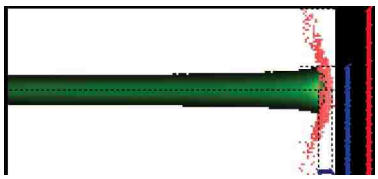

Figure 5.6: 150 $[MeV]$ proton beam. *In green:* dose deposition. *In red:* LET.

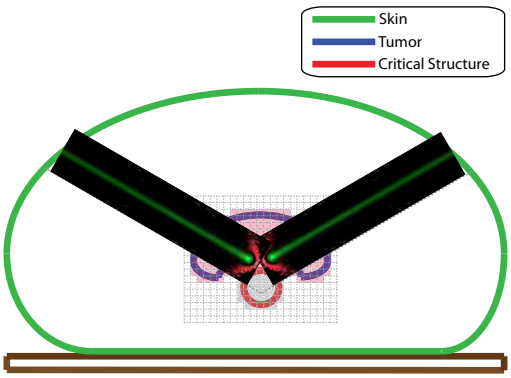

Figure 5.7: Two proton beams interacting with a phantom. *In green:* dose deposition. *In red:* LET deposition.

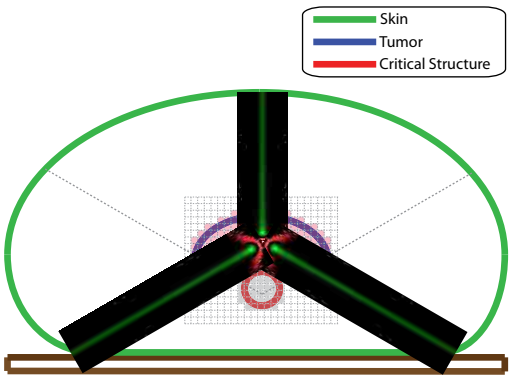

Figure 5.8: Three proton beams interacting with a phantom. *In green:* dose deposition. *In red:* LET desposition.

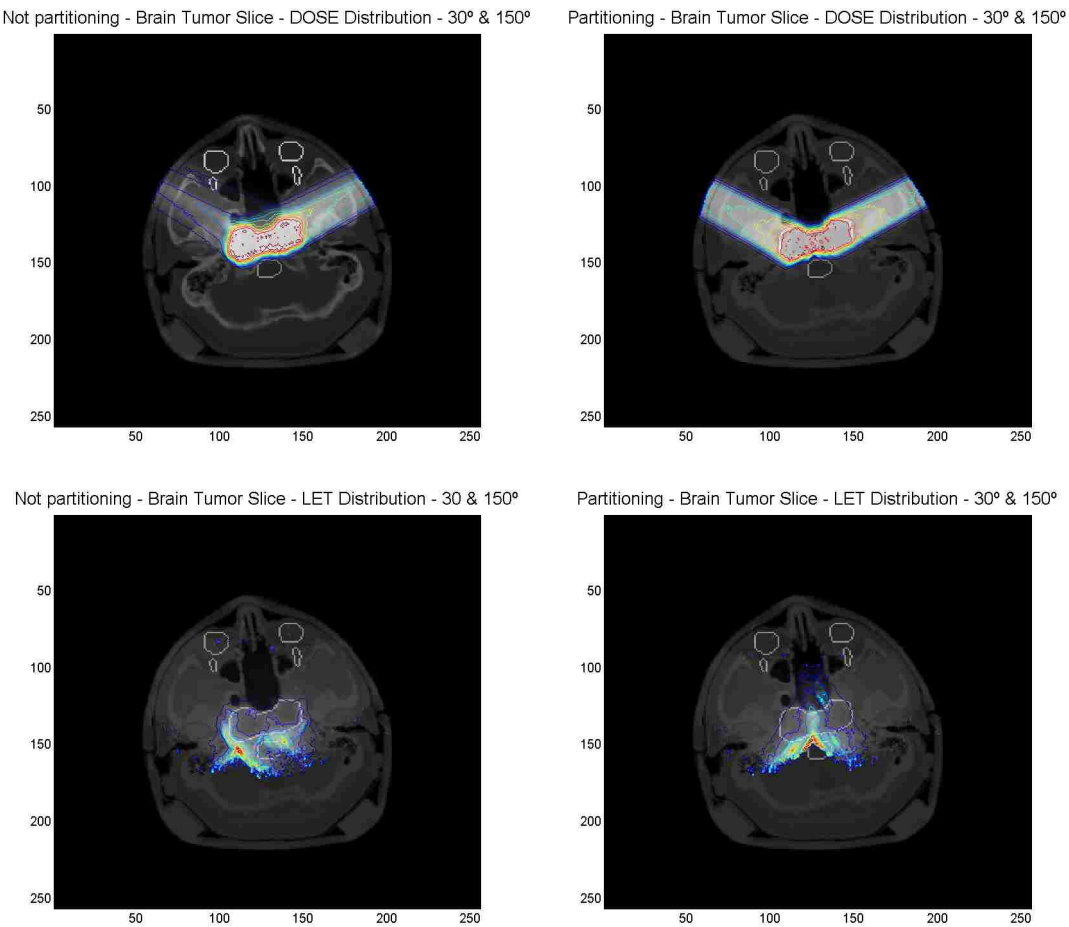

Figure 5.9: Brain tumor case for 30° and 150° beam angles. *Top left:* dose distribution for normal optimization without partitioning. *Top right:* dose distribution using Voronoi partitioning. *Bottom left and right:* LET distributions for each case respectively.

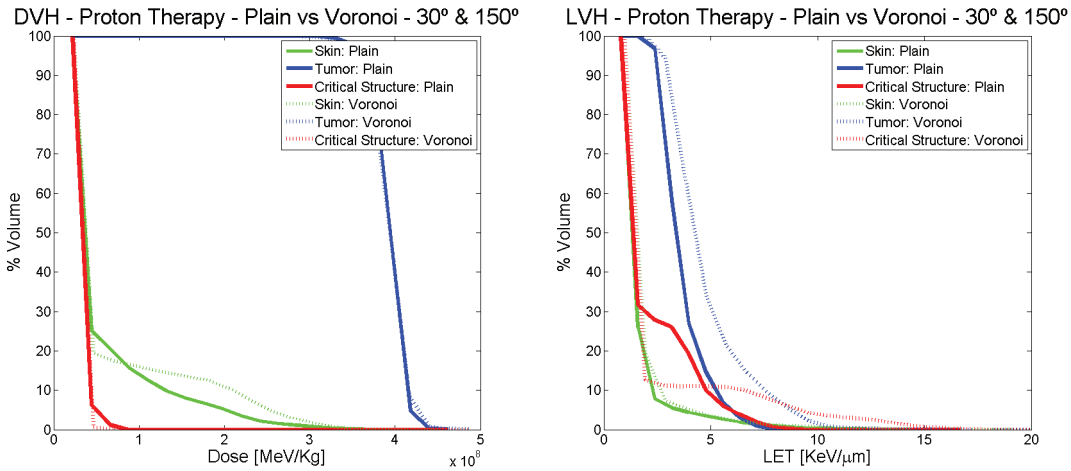

Figure 5.10: DVH & LVH comparison of both treatment plans (for 30° and 150° beam angles): Plain vs. Voronoi.

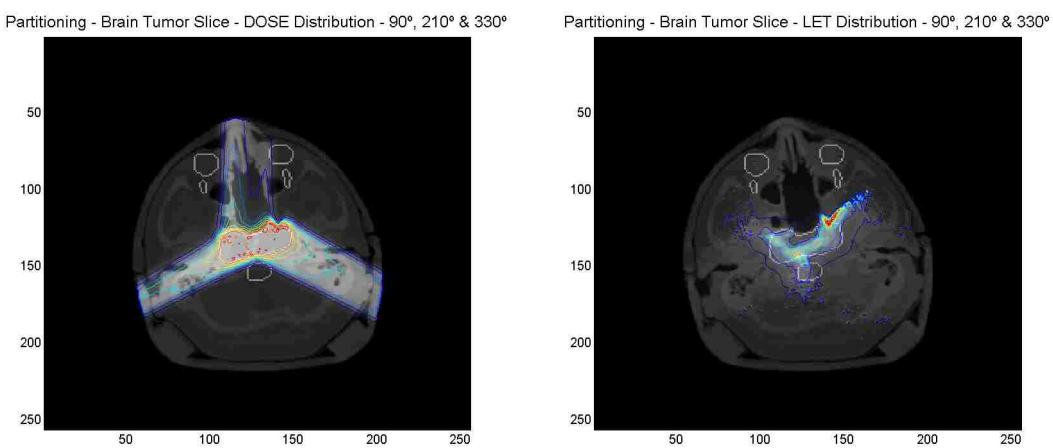

Figure 5.11: Brain tumor case for 90°, 210° & 330° beam angles. *Left:* dose distribution using Voronoi partitioning. *Right:* LET distribution using Voronoi partitioning.

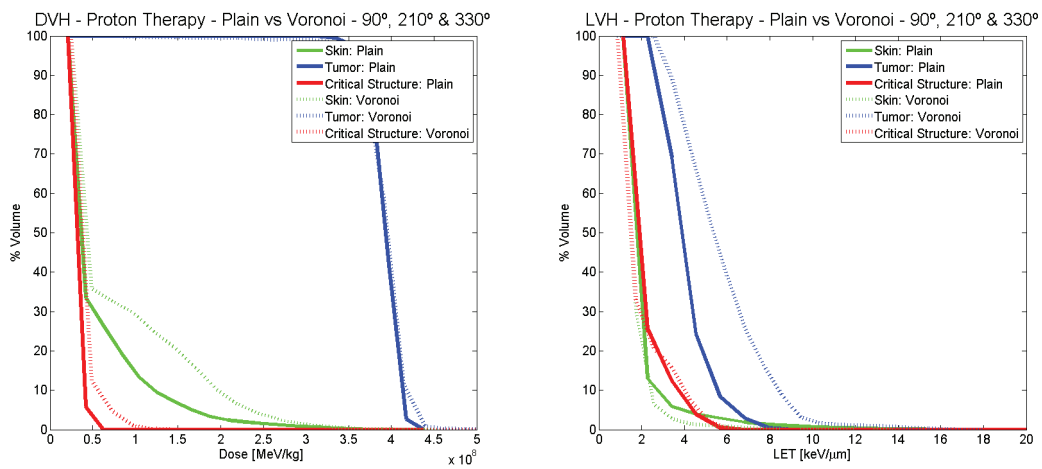

Figure 5.12: DVH & LVH comparison of both treatment plans (for 90°, 210° & 330° beam angles): Plain vs. Voronoi.

Chapter 6

Conclusions and Future Work

6.1 Conclusion

In this thesis, we have developed a prototype planning system for particle therapy, and applied Voronoi partitions to help solving the energy modulation change reduction problem and the LET painting problem. Our prototype experiments indicate that Voronoi partitions can be an effective mechanism for solving such problems. In the case of energy change reduction, the number of energy changes can be reduced by as much as 70% while maintaining similar dosimetric qualities. For LET painting, a desired LET is observed inside the target, and dose and LET distributions are simultaneously optimized.

6.2 Future work

This thesis provides a valuable learning experience of particle therapy, and helps to identify an array of exciting computational problems for my future PhD dissertation.

Below, I would like to sketch some of the problems that we will be investigating in the near future.

6.2.1 Treatment planning system prototype

In terms of enhancements of our treatment planning system prototype, we have identified the following enhancements:

- *Loader:* investigate the use of hash tables and file cache schemes to improve the manipulation of dose kernels.
- *Pre-process:* explore incremental algorithms for Voronoi partitioning as well as GPU-based algorithms.
- *Dose Calculation:* explore new ray-tracing algorithms in order to increase data locality to avoid redundant calculations.

6.2.2 Beam energy modulation minimization

While studying this problem, we came across an interesting computational geometry problem that requires further studying. If we consider the patient anatomy as a polyhedron for a given set of beam angles (lines), minimizing the beam energy modulation means to minimize the sum of the polyhedron projections onto the provided beam angles which can also be seen as a polyhedron partitioning algorithm. The following discussion states the two-dimensional formulation of this problem which is helpful to understand in order to generalize for the general case and specially to find a solution and runtime bounds for the three-dimensional case.

Definition 1 *Given a simply polygon P, and a direction specified by a straight line l, we denote the projection of P with respect to l as the line segment $l(P)$ obtained*

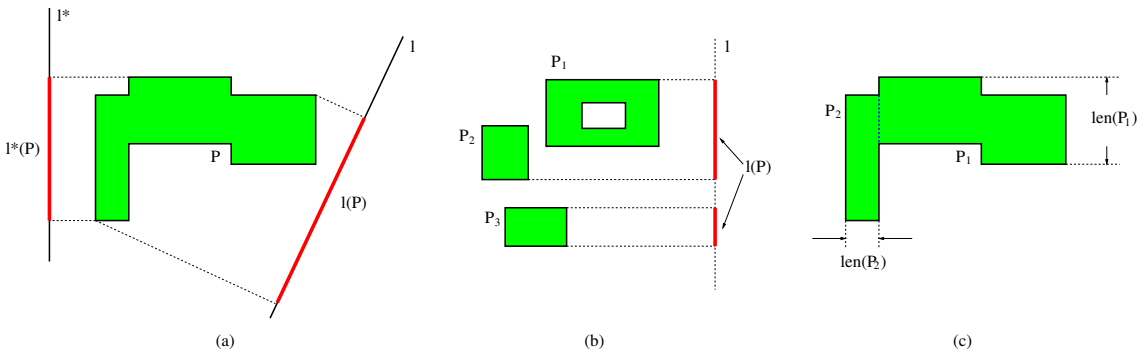

Figure 6.1: (a) Illustration of the projection length of a polygon with respect to a line direction. (b) illustration of the projection of a polygonal domain $P = P_1 \cup P_2 \cup P_3$. Notice that the polygon P_1 also contains a hole. (c) Illustration of the optimal partition.

when P is projected onto l. Figure 6.1 (a) illustrates the projection of a polygon P onto two lines l^* and l. The length of $l(P)$, denoted by $|l(P)|$ is called the projection length of P with respect to l.

Definition 2 *Definition 1 can be extended to a polygon domain P consisting of a collection of simple polygons $P_1, P_2, ..., P_k$ possibly with holes. Figure 6.1 (b) illustrates the projection of three polygons P_1, P_2, and P_3 onto line l. In the case of a polygonal domain, the projection with respect to a line direction l can consist of a set of disjoint line segments, and its projection length the sum of the total lengths of these line segments.*

Definition 3 *The projection length (or just length) of a polygon P, denoted by $len(P)$ is defined to be the minimum length of P over all possible directions, i.e., $len(P) = \min_l |l(P)|$. We use l^* to denote the direction such that $|l^*(P)| = len(P)$. Figure 6.1 (a) shows the projection length of a simple polygon, where l^* is the line direction that achieves the projection length of P.*

As part of our future work on beam energy modulation reduction, we propose the study of the following polygon partitioning problems:

Problem 1 *Given a polygon P, partition P into its k minimum number of pieces $P_1, P_2, ..., P_k$ (each piece can be a simple polygon or a polygonal domain), such that $\sum_{i=1}^{k} len(P_i)$ is minimized. (See figure 6.1 (c) for illustrations).*

We are also interested in the following dual version of the problem:

Problem 2 *Given a polygon P and a positive integer K. Partition P into at most K pieces, i.e., $P_1, P_2, ..., P_k$, and $k \leq K$, such that $\sum_{i=1}^{k} len(P_i)$ is minimized.*

Besides the above two problems, the following problem is also of important clinical value:

Problem 3 *Given a polygon P and a set of directions $S = \{l_1, l_2, ..., l_K\}$. Partition P into K pieces, i.e., $P_1, P_2, ..., P_K$ (each piece can be empty), such that $\sum_{k=1}^{K} |l_k(P_k)|$ is minimized. (See Figure 6.2 for illustrations.)*

Observe that one can reduce Problems 1 and 2 to Problem 3 by letting the set S contain all possible beam directions. Notice as well that Problem 3 resembles a classical problem in Computer Science: *set cover problem* of which the decision version is known to be NP-complete [43, 49].

6.2.3 Simultaneous Dose & LET painting

This particular problem can be understood in two different ways: targeting a high LET inside a particular region inside the tumor or enhancing LET concentration

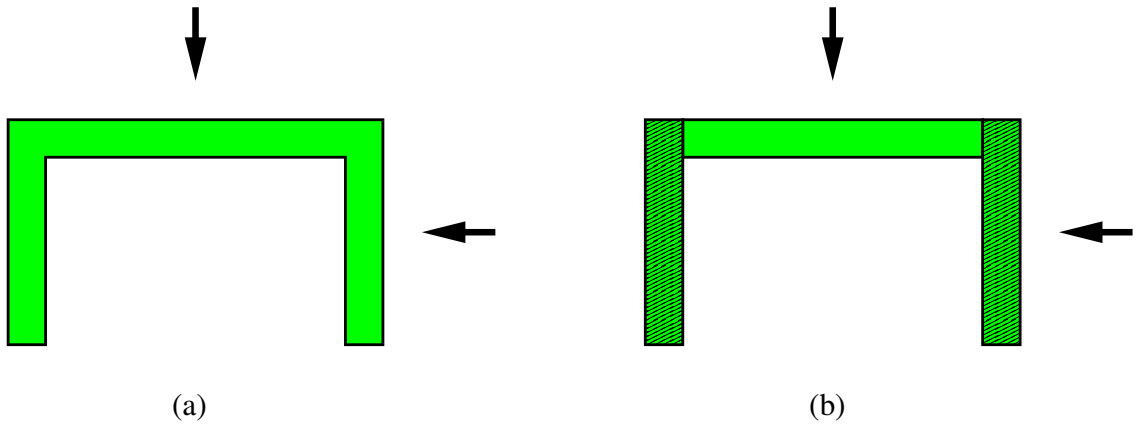

Figure 6.2: Illustrating Problem 3. (a) A polygon and two given beam directions. (b) Illustrating the partition of the given polygon into two pieces, where the region with the patterns is aligned with the horizontal beam direction, and the rest is aligned with the vertical beam direction.

in the tumor while avoiding organs at risk. Although, both seem to target similar objective functions the first one by itself defines a region that can be modeled as problem 1, 2, and 3 where we can partition the tumor such that the selected beams stop inside these particular regions inside the tumor. The second version of the problem can be solved by using a constraint least squares optimization using the connection between dose and LET in order to express dose constraints in terms of LET.

6.2.4 Integrated Beam Angle Selection

Our current formulations of the beam energy modulation minimization and the simultaneous dose & LET painting problems rely on a set of given beam angles to find a good solution in terms of dose conformity and/or LET enhancement. The limitation of this approach is that some beam angles might decrement the quality of the solution (i.e. adding unnecessary energy changes or diluting LET concentra-

tion), then a combined strategy that integrates beam angle selection is desirable. Hence, the beam angle selection problem integrated to our problems can be stated as: "Given a set of k beam angles, find the Voronoi partition with $2 \leq k$ sites, such that a high quality dose treatment plan is obtained while minimizing the amount of energy changes or maximizing the LET concentration inside the tumor".

References

[1] D. Schardt, T. Elsässer, and D. Schulz-Ertner, *Heavy-ion tumor therapy: Physical and radiobiological benefits*, Rev. Mod. Phys. **82** (2010), 383–425.

[2] E. J. Hall and A. J. Giaccia, *Radiobiology for the Radiologist*, Lippincott Williams & Wilkins, 2006.

[3] F. M. Khan, *The Physics of Radiation Therapy*, Lippincott Williams & Wilkins, 2010.

[4] F. Aurenhammer, *Voronoi diagrams: a survey of a fundamental geometric data structure*, ACM Comput. Surv. **23** (1991), 345–405.

[5] Z. Chen *Dynamic photon painting* Master's thesis, University of New Mexico, 2010.

[6] O. Jäkel, C. Jacob, D. Schardt, C. P. Karger, and G. H. Hartmann, *Relation between carbon ion ranges and x-ray ct numbers* **28** (2001), 701–703.

[7] W. Schneider, T. Bortfeld, and W. Schlegel, *Correlation between ct numbers and tissue parameters needed for monte carlo simulations of clinical dose distributions*, Physics in Medicine and Biology **45** (2000), 459.

[8] D. J. Griffiths, *Introduction to Elementary Particles*, Wiley, John & Sons, Inc., 1987.

[9] S. Agostinelli, J. Allison, K. Amako, J. Apostolakis, H. Araujo, P. Arce, M. Asai, D. Axen, S. Banerjee, G. Barrand, F. Behner, L. Bellagamba, J. Boudreau, L. Broglia, A. Brunengo, H. Burkhardt, S. Chauvie, J. Chuma, R. Chytracek, G. Cooperman, G. Cosmo, P. Degtyarenko, A. Dell'Acqua, G. Depaola, D. Dietrich, R. Enami, A. Feliciello, C. Ferguson, H. Fesefeldt, G. Folger, F. Foppiano, A. Forti, S. Garelli, S. Giani, R. Giannitrapani, D. Gibin, J. J. G. Cadenas, I. Gonzlez, G. G. Abril, G. Greeniaus, W. Greiner, V. Grichine, A. Grossheim, S.

Guatelli, P. Gumplinger, R. Hamatsu, K. Hashimoto, H. Hasui, A. Heikkinen, A. Howard, V. Ivanchenko, A. Johnson, F. W. Jones, J. Kallenbach, N. Kanaya, M. Kawabata, Y. Kawabata, M. Kawaguti, S. Kelner, P. Kent, A. Kimura, T. Kodama, R. Kokoulin, M. Kossov, H. Kurashige, E. Lamanna, T. Lampn, V. Lara, V. Lefebure, F. Lei, M. Liendl, W. Lockman, F. Longo, S. Magni, M. Maire, E. Medernach, K. Minamimoto, P. M. de Freitas, Y. Morita, K. Murakami, M. Nagamatu, R. Nartallo, P. Nieminen, T. Nishimura, K. Ohtsubo, M. Okamura, S. O'Neale, Y. Oohata, K. Paech, J. Perl, A. Pfeiffer, M. G. Pia, F. Ranjard, A. Rybin, S. Sadilov, E. D. Salvo, G. Santin, T. Sasaki, N. Savvas, Y. Sawada, S. Scherer, S. Sei, V. Sirotenko, D. Smith, N. Starkov, H. Stoecker, J. Sulkimo, M. Takahata, S. Tanaka, E. Tcherniaev, E. S. Tehrani, M. Tropeano, P. Truscott, H. Uno, L. Urban, P. Urban, M. Verderi, A. Walkden, W. Wander, H. Weber, J. P. Wellisch, T. Wenaus, D. C. Williams, D. Wright, T. Yamada, H. Yoshida, and D. Zschiesche, *G4–a simulation toolkit*, Nuclear Instruments and Methods in Physics Research Section A: Accelerators, Spectrometers, Detectors and Associated Equipment **506** (2003), 250 – 303.

[10] J. Allison, K. Amako, J. Apostolakis, H. Araujo, P. Dubois, M. Asai, G. Barrand, R. Capra, S. Chauvie, R. Chytracek, G. Cirrone, G. Cooperman, G. Cosmo, G. Cuttone, G. Daquino, M. Donszelmann, M. Dressel, G. Folger, F. Foppiano, J. Generowicz, V. Grichine, S. Guatelli, P. Gumplinger, A. Heikkinen, I. Hrivnacova, A. Howard, S. Incerti, V. Ivanchenko, T. Johnson, F. Jones, T. Koi, R. Kokoulin, M. Kossov, H. Kurashige, V. Lara, S. Larsson, F. Lei, O. Link, F. Longo, M. Maire, A. Mantero, B. Mascialino, I. McLaren, P. Lorenzo, K. Minamimoto, K. Murakami, P. Nieminen, L. Pandola, S. Parlati, L. Peralta, J. Perl, A. Pfeiffer, M. Pia, A. Ribon, P. Rodrigues, G. Russo, S. Sadilov, G. Santin, T. Sasaki, D. Smith, N. Starkov, S. Tanaka, E. Tcherniaev, B. Tome, A. Trindade, P. Truscott, L. Urban, M. Verderi, A. Walkden, J. Wellisch, D. Williams, D. Wright, and H. Yoshida, *Geant4 developments and applications*, Nuclear Science, IEEE Transactions on **53** (2006), 270 –278.

[11] W. Wieszczycka and W. H. Scharf, *Proton Radiotherapy Accelerators*, World Scientific, 2001.

[12] A. C. Society, *Cancer facts & figures 2011*, Atlanta: American Cancer Society.

[13] ———, *Cancer facts & figures 2010*, Atlanta: American Cancer Society.

[14] J. J. Wilkens and U. Oelfke.

[15] J. Wilkens and U. Oelfke, *Analytical linear energy transfer calculations for proton therapy.*, Med Phys **30** (2003), 806–15.

[16] J. J. Wilkens and U. Oelfke, *A phenomenological model for the relative biological effectiveness in therapeutic proton beams*, Physics in Medicine and Biology **49** (2004), 2811.

[17] N. Bassler, O. Jäkel, C. S. Sondergaard, and J. B. Petersen.

[18] C. Grassberger, A. Trofimov, A. Lomax, and H. Paganetti, *Variations in linear energy transfer within clinical proton therapy fields and the potential for biological treatment planning*, International Journal of Radiation Oncology*Biology*Physics **80** (2011), 1559 – 1566.

[19] R. A. Novelline, *Squire's Fundamentals of Radiology: Sixth Edition*, Harvard University Press, 2004.

[20] H. Becquerel, *Sur les radiations émises par phosphorescence (on the invisible rays emitted by phosphorescent bodies)*, Comptes rendus de l'Académie des Sciences **122** (1896), 420–421.

[21] M. P. C. P. Curie and G. Bémont, *Sur une nouvelle substance fortement radioactive, contenue dans la pechblende)*, Comptes rendus de l'Académie des Sciences **127** (1898), 1215–1217.

[22] F. H. Attix, *Introduction to Radiological Physics and Radiation Dosimetry*, WILEY-VCH, 2004.

[23] P. M. Pardalos and H. Romeijn, *Handbook of Optimization in Medicine*, Springer, 2008.

[24] M. Goitein, *Radiation Oncology: A Physicist's-Eye View*, Springer, 2008.

[25] G. Kraft, *Rbe and its interpretation*, Strahlentherapie und Onkologie **175** (1999), 44–47 (10.1007/BF03038887).

[26] P. Mayles, A. Nahum, and J. Rosenwald, *Handbook of Radiotherapy Physics: Theory and Practice*, CRC Press, 2007.

[27] M. Joiner and A. van der Kogel, *Basic Clinical Radiobiology: Fourth Edition*, Hodder Arnold, 2009.

[28] N. Metropolis and S. Ulam, *The Monte Carlo method* **44** (1949), 335–341.

[29] H. Jiang, J. Seco, and H. Paganetti, *Effects of hounsfield number conversion on ct based proton monte carlo dose calculations.*

[30] T. F. DeLaney and H. M. Kooy, *Proton and Charged Particle Radiotherapy*, Lippincott Williams & Wilkins, 2008.

[31] C. L. Lawson and R. J. Hanson, *Solving Least Squares Problems*, SIAM, 1995.

[32] R. R. Wilson, *Radiological Use of Fast Protons*, Radiology **47** (1946), 487+.

[33] M. Krämer, O. Jäkel, T. Haberer, G. Kraft, D. Schardt, and U. Weber, *Treatment planning for heavy-ion radiotherapy: physical beam model and dose optimization*, Physics in Medicine and Biology **45** (2000), 3299–3317.

[34] G. Battistoni, S. Muraro, P. Sala, F. Cerutti, A. Ferrari, S. Roesler, A. Fasso, and J. Ranft, *The fluka code: Description and benchmarking*, Proceedings of the Hadronic Shower Simulation Workshop 2006.

[35] A. Fasso, A. Ferrari, J. Ranft, and P. Sala, *Fluka: a multi-particle transport code*, Proceedings of the Hadronic Shower Simulation Workshop 2006.

[36] M. de Berg, O. Cheong, M. van Kreveld, and M. Overmars, *Computational Geometry, Algorithms and Applications*, Springler, 2008.

[37] K. H. Rosen, *Handbook of Discrete and Computational Geometry*, Chapman & Hall/CRC, 2004.

[38] F. P. Preparata and M. I. Shamos, *Computational Geometry: An Introduction*, Springer-Verlag, 1985.

[39] A. Okabe, B. Boots, K. Sugihara, and S. N. Chiu, *Spatial Tessellations: Concepts and Applications of Voronoi Diagrams*, John Wiley & Sons, LTD., 2000.

[40] F. Aurenhammer and R. Klein, *Voronoi Diagrams - Aurenhammer, Klein*, Elsevier Publishing House, 1999, Chap. 5, pp. 201–290.

[41] Q. Du, V. Faber, and M. Gunzburger, *Centroidal voronoi tessellations: Applications and algorithms*, SIAM Rev. **41** (1999), 637–676.

[42] M. I. Shamos, *Computational Geometry*, PhD thesis, Ph.D. thesis, Department of Computer Science, Yale University, 1978.

[43] T. H. Cormen, C. E. Leiserson, R. L. Rivest, and C. Stein, *Introduction to Algorithms, Second Edition*, The MIT Press, 2001.

[44] V. Klee, *Archiv der Mathematik, On the complexity of d-dimensional Voronoi diagrams*, Springler, 1980, pp. 75–80.

[45] P. J. Green and R. R. Sibson, *Computing dirichlet tessellations in the plane*, Comput. J.

[46] S. Fortune, *A sweepline algorithm for voronoi diagrams*, in Proceedings of the second annual symposium on Computational geometry, SCG '86, ACM, New York, NY, USA, 1986, pp. 313–322.

[47] M. I. Shamos and D. Hoey, *Closest-point problems*, in In Proc. 16th Annu. IEEE Sympos. Found. Comput. Sci., 1975, pp. 151–162.

[48] K. E. Hoff, III, T. Culver, J. Keyser, M. Lin, and D. Manocha, *Fast computation of generalized voronoi diagrams using graphics hardware*, in Proceedings of the sixteenth annual symposium on Computational geometry, SCG '00, ACM, New York, NY, USA, 2000, pp. 375–376.

[49] S. S. Skiena, *The Algorithm Design Manual: Second Edition*, Springer, 2008.